Thermal and Electrical Performances of Semi-Transparent Photovoltaic Glazing Integrated with Translucent Vacuum Insulation Panel and Vacuum Glazing

Ali Radwan,[1, 2*] Takao Katsura,[1] Saim Memon,[3] Ahmed A. Serageldin,[1,4] Makoto Nakamura,[1] Katsunori Nagano[1]

[1]Division of Human Environmental Systems, Faculty of Engineering, Hokkaido University, Japan.

[2]Mechanical Power Engineering Department, Faculty of Engineering, Mansoura University, El Mansoura 35516, Egypt.

[3]London Centre for Energy Engineering, School of Engineering, London South Bank University, 103 Borough Road, London, SE1 0AA, UK.

[4]Mechanical Power Engineering Department, Faculty of Engineering at Shoubra, Benha University, Shoubra 11629, Egypt

[*]Corresponding Author: Ali Radwan

Division of Human Environmental Systems, Faculty of Engineering, Hokkaido University, Japan.
Address:- Division of Human Environmental Systems, Faculty of Engineering, Hokkaido University, N13-W8, Kita-ku, Sapporo 060-8628, Japan
Email: Ali.radwan@ejust.edu.eg
Tel: +81-11-706-6284

Abstract

The development of smart windows for residential and commercial buildings is an attractive way to decrease energy consumption in this sector. These windows must provide low solar heat gain with a low overall heat transfer coefficient, avoid humidity and condensation in cold regions, generate clean electricity, and admit comfortable levels of daylight. Therefore, methods for integrating semi-transparent (or 50.8% transparent) CdTe solar cell strings-based glazing with structured-cored mesh translucent vacuum insulation panels and indium sealed vacuum glazing are described for modernizing smart windows. This paper contributes to the net zero-energy building concept, an aspect of a global industrial strategy for climate-change mitigation. This study reports experimental and theoretical studies on the thermal and electrical performances of six different glazing systems. These systems include semi-transparent photovoltaic glazing (GPV), vacuum glazing (VG), translucent vacuum insulation panel (GVIP), semi-transparent PV with VG (VGPV), and semi-transparent PV with translucent vacuum insulation panel (VIPPV), and their performances will be compared with that seen with single glazing (SG). These glazing systems are designed, constructed, and tested using a hot box calorimeter, and with and without the effects of simulated indoor solar radiation. The center-of-pane U-values, the transient temperature variations of the inner and outer surfaces of the glazing systems, the open circuit voltages, the short circuit currents, the fill factors, and the steady-state temperature contours were determined experimentally with the use of an infrared camera. For the first time, the moisture condensation pattern is also depicted for these systems and will be of value for applications in harsh, cold regions. A 3D finite-volume heat transfer model is developed and validated with the experimental results, allowing comparison of the thermal performances of these glazing systems under ASTM boundary conditions. The results showed that the VGPV system achieved a lower U-value than did the VIPPV system. The steady-state center-of-pane temperature differences seen with a solar irradiation level of 1000 $W \cdot m^{-2}$ are 55 ºC, 32.5 ºC and 5 ºC for the VGPV, VIPPV, and GPV systems, respectively. The validated center-of-pane U-values for the VG, VGPV, VIPPV, and GPV systems, each with dimensions of 15 cm × 15 cm, are predicted to be 1.3, 1.2, 1.8, and 6.1 $W \cdot m^{-2}K^{-1}$, respectively. The results also show that the use of either the VGPV or VG systems eliminates moisture condensation. It is concluded that VGPV and VIPPV generate comparatively less power but provide higher thermal insulation.

Keywords: Semi-transparent CdTe photovoltaics; translucent vacuum insulation panel; vacuum glazing; 3D finite-volume modeling; thermal and electrical performances.

1. Introduction

Advancements in progressive vacuum insulation technologies are believed to be one of the more realistic solutions for converting domestic and commercial buildings into nearly zero-energy buildings (NZEBs) and/or zero energy buildings (ZEBs) and could contribute to the realization of net-zero carbon emissions by 2050. It is widely accepted that, in the building sector, energy losses/gains through windows account for more than 30% of energy consumption, more than that of any other building element [1]. In addition, a significant increase in the fraction of high-rise buildings constructed with large transparent facades requires the integration of progressive novel technologies in the smart window sector [2]. Therefore, Building Integrated Photovoltaic (BIPV) technologies have become one of the most promising options for meeting the needs of these sectors, since energy generation is also advantageous [3]. In BIPV, the problems of large land requirements and transmission power losses are avoided by integrating the photovoltaic (PV) arrays on the exterior facades of the buildings [4]. Further, designers in the building sector are recognizing that NZEBs must rely on the use of PV systems, along with building envelope insulation technologies [5]. The PV system generates electricity for building needs and decreases the solar heat gain emerging from the building or striking the outside surfaces [4]. The thermal insulation for exterior transparent facades plays an essential role in reducing the thermal heat loss and raising energy requirements, particularly with large window-to-wall ratios in high-rise buildings [6]. Therefore, using hybrid semi-transparent PVs with higher thermal insulation efficiency is an effective way to provide both power generation and thermal insulation without compromising the facade area [7].

1.1. Semi-transparent Photovoltaic (STPV) glazing

In the building integrated photovoltaic (BIPV) sector, lamination of the glass sheet to an STPV layer is used to replace the conventional low-e coated single-glazed window. This helps to reduce the transmittance of solar radiation through the PV laminate area, and, consequently, reduces the building heat gain [1]. Lu and Law [8] proposed a detailed one-dimensional transient heat transfer model for STPV double glazing consisting of a polycrystalline silicon solar cell fixed between two transparent glass panes. In these structures, the silicon wafer generates electricity. However, due to the opaque characteristics of the silicon wafer, the solar cell constitutes a certain fraction of the total glazing area; this is called the 'coverage ratio,' and it amounts to 60% of the glazing area. The ratio of solar cell area to the total glazing area (coverage ratio) has a significant effect on the total heat gain of buildings. STPV-based cadmium telluride (CdTe) glazed windows are used in [9], in which the CdTe cell coverage ratio was 10%. Peng et al. [1] introduced a novel c-Si-based STPV glazing. This was produced by cutting multiple strips of standard c-Si solar cells, which were automatically welded and electrically connected into continuous strings. These strings were laminated between two glass layers, and the c-Si wafers were embedded in two layers of polyvinyl butyral (PVB) with a thickness of 0.5 mm above and below the c-Si layer.

In the area of STPV glazing, different types of solar cells have been used; these include amorphous silicon (a-Si) [10], cadmium telluride (CdTe) thin-film [9], dye-sensitized solar cells [11], amorphous silicon [12] and crystalline silicon solar cells (c-Si) [13]. In c-Si solar cells using STPV, the silicon wafer is embedded in an ethylene-vinyl acetate (EVA) or PVB layer and surrounded by glass panes on both sides [13]. The non-reflected irradiation is transmitted through the gaps between solar cell layers to the indoor space, and this allows subsequent passive heating; this is useful during the winter season but may cause overheating during summer months, especially in hot-arid regions [14]. Additionally, the solar absorbance of the silicon wafer can lead to higher temperatures in the solar cell domain in hot-arid regions. There remain two significant issues that were not comprehensively investigated in these or other studies.

First, the solar radiation absorbed in the solar cells is partially converted to electric power, with up to 20% conversion efficiency, and the rest of the absorbed light is converted into heat in the solar cell [15]. This generated heat causes a significant increase in the solar cell temperature and decreases its service life. Additionally, this temperature increase results in transfer of considerable heat into the building via conduction through the STPV glazing, especially in hot areas. This results in an increase in the thermal heat gain for the building. Second, for extreme cold-arid regions there are considerable gaps in the knowledge regarding STPV thermal insulation performance and indoor moisture condensation. This is because the interior temperature of the window surface may be lower than the dew point temperature of the inside air. This moisture condensation problem lowers visibility and raises the issue of fungal and bacterial growth, which negatively affects the occupants' health and comfort. Therefore, this paper also presents investigations of these aspects, which do not appear in prior literature.

1.2. Transparent insulation materials (TIMs) for transparent facades

Conventional windows cause higher thermal heat loss/gain to/from the outside in the cold-arid and the hot-arid climates, respectively. These windows typically consist of 6 mm thick single-glazed windows with a U-value (thermal transmittance) of 5.7 $W{\cdot}m^{-2}\,K^{-1}$ [6], or, with current trends in triple air-filled glazed windows, can achieve a U-value of 1.8 $W{\cdot}m^{-2}\,K^{-1}$. Recently, TIMs for exterior facades have offered the potential to enhance building performance [2]. These TIMs are used to offer heat transfer resistance while also facilitating light transmission. The TIMs described in the literature were reviewed thoroughly in [2]. The TIMs described in the literature are assembled with at least one transparent cover, typically glass with an air cavity between the panes of a double-pane glazing unit [2]. Some examples of these TIMs are the vacuum glazing systems (VG) [16] and transparent vacuum insulated panels (TVIPs) [17].

The VG system consists of two glass panes separated by an array of support pillars (approximately 0.13 mm in length and 0.3 mm in diameter), in which an evacuated gap with a pressure less than 0.1 Pa is established using a hermetic edge seal [18]. The VG exhibits good thermal transmittance values (U-values) ranging between 1.1 $W{\cdot}m^{-2}\,K^{-1}$ and 0.8 $W{\cdot}m^{-2}\,K^{-1}$ with a vacuum pressure of less than 0.1 Pa [19]. However, for smaller VG systems, the thermal performance of the system is partially diminished by edge effects [20].

This results because the edge seal is made with a highly conductive sealing material, with a thermal conductivity of approximately 87.3 $W \cdot m^{-1} K^{-1}$ seen for typical indium-sealed VG systems [20]. This conductive material provides a thermal short circuit around the edges and increases the total glazing U-value [21]. The lower U-value for VG systems could prevent indoor moisture condensation, but proof of this notion has not yet appeared in the literature.

Conversely, conventional vacuum insulation panels (VIPs) have lower thermal conductivities, typically ranging between 0.004 $W \cdot m^{-1} K^{-1}$ and 0.008 $W \cdot m^{-1} K^{-1}$ [22]. These conventional VIPs consist of an aluminum gas barrier film with opaque characteristics and a solid core thermal insulating material, which is usually kept inside this gas barrier film and thermally sealed after evacuation [23]. The U-values of VIPs range from 0.1 $W \cdot m^{-2} K^{-1}$ to 0.3 $W \cdot m^{-2} K^{-1}$ [24]. The inner core material in the conventional VIP is usually constructed with an evacuated porous-core material such as fumed silica [23], polycarbonate [25], phenolic foam [26], glass fiber [27], and/or fibrous powder [28]. The aluminum gas barrier envelope maintains a vacuum pressure of about 10 Pa [29] and minimizes the heat transfer through the outside cover normally caused by gas molecules and water vapor. Because of the non-transparent nature of conventional VIPs, they cannot be utilized for windows because of the requirements for transparency and visible light transmission. Conventional VIP sealing is easier than is sealing with the VG. There is a considerable need for a cost-effective and transparent thermal insulation option that does not exhibit edge sealing effects and is easily retrofitted into existing buildings. The construction of translucent VIPs and the concept of VIPs with negligible thermal edge effects, particularly with the application for PV windows, have not appeared in the literature. This study is designed to utilize opaque thermal characteristics for the realization of a new structured-core translucent VIP.

Table 1: Summary of the recent investigations for the semi-transparent PV glazed windows

Authors, year	Ref	Study*		Semi-transparent PV glazing structure	Testing**		Solar cell type	Measured or predicted parameters	Simulation tool	Conclusions
		Exp.	Th.		I	O				
Ghosh et al. 2019	[4]	---	✓	1- BIPV-VG (Glass/PV/Glass/vacuum /Glass) 2- BIPV-double glazing (Glass/PV/Glass)	✓	✓	Crystalline silicon (c-Si) solar cell	1- Solar cell temperature 2- Room temperature 3- Internal glass temperature	MATLAB, Energy balance model	1- PV cell temperature in the case of BIPV-VG is higher than that for double pane glazing by 24 ºC. 2- BIPV-VG accomplished 26% higher room temperature compared to BIPV-double glazing.
Qiu et al., 2019	[10]	---	✓	Glass/PV/glass/VG, PV facing outdoor	--	✓	amorphous silicon (a-Si)	Energy consumption for different lactations	EnergyPlus Energy balance model	1- They concluded that the vacuum PV glazing system provided a substantial energy-saving potential in cold winter and hot summer regions. 2- It is not favorable for the moderate climatic regions.
Cuce & Cuce, 2019	[12]	✓	✓	Thermally resistive PV glazing TRPVG. Nanocoating/PV/ argon gap/ L-e coating/ thermal resistive glass	✓	--	amorphous silicon (a-Si)	Temperature distribution and heat loss	ANSYS FLUENT, 3D	1- For the TRPVG sample with an argon gap of 16 mm, the total U-value was approximately 1.19 $W \cdot m^{-2} K^{-1}$. 2- The optimized value of the argon gap is determined to be 20 mm.
Ghosh et al., 2018	[13]	✓	---	1- VG / PV/ single glazing/room (VPS) 2- SG / PV/ VG/room (SPV) 3- SG / PV/ single glazing/room (SPS)	✓	--	Crystalline silicon (c-Si) solar cell	1- Solar cell temperature 2- Room temperature 3- Internal glass temperature 4- U-value 5- Electrical parameters	---	1- SPV system achieved a lower temperature than VPS at 1000 $W \cdot m^{-2}$ simulated solar light. 2- For the SPV-VG, the overall heat transfer coefficient (U-value) was 0.8 $W \cdot m^{-2} K^{-1}$. This U-value of was 66% lower than SPS glazing. 3- The maximum achieved PV cell temperature was around 97 °C under 1000 $W \cdot m^{-2}$ simulated light.

Sun et al., 2018	[9]	---	✓	1- Double glazing 2- CdTe window	--	✓	Thin film CdTe solar cells	Energy consumption	EnergyPlus, 0D	1- Comparing the CdTe and the double-glazed system, the application of the PV window can result in a considerable reduction in energy consumption by up to 73%.
Park et al., 2010	[30]	✓	---	Glass-PV-glass-air gap-glass system	--	✓	Crystalline silicon solar cell	Solar cell temperature And electrical parameters	---	1- The air gap temperature was the highest and followed by the PV cell. 2- Its temperature influenced the electrical generation of the PV cell. They confirmed that the generated power of the PV module decreased about 0.48% per 1 °C increase in the indoor test and decreased approximately 0.52% per 1 °C increase in the outdoor test at a solar radiation of 500 $W \cdot m^{-2}$.
Kang et al. 2003	[11]	✓	---	Single-layer of the solar cell	✓	--	dye-sensitized nanocrystalline TiO_2 solar	Solar cell electrical characteristics	---	1- They manufactured a transparent solar cell with an area of $8 \times 8\ cm^2$ active area. The transmittance of the solar cell was about 60% in the visible range. 2- The measured open-circuit voltage (V_{oc}) and short circuit current (I_{sc}) were about 0.64 V and 250 mA, respectively. 3- For scale-up, nine-unit of this solar cell to compose semi-transparent window generated V_{oc} of 5.7 V and I_{sc} of 220 mA at 1000 $W \cdot m^{-2}$ light intensity.

*(Th: theoretical; Exp: Experimental); **(I: indoor testing; O: outdoor testing condition)

1.3. Hybrid semi-transparent PV insulated windows

There is significant promise for integrating the progressive vacuum insulation technologies with semi-transparent PV glazing to modernize the building sector and realize higher energy efficiency [16]. The energy-efficient windows (EEW) of today generate electricity and exhibit very low U-values. This is accomplished by combining hybrid semi-transparent PVs with a transparent thermal insulation method. The consolidation of the semi-transparent PV modules allows control of the solar heat gain coefficient in hot-arid regions. However, it also brings the disadvantage of increased building cooling load resulting from the transmittance of the remaining solar radiation. Therefore, to provide excellent thermal insulation for the windows, the VG integration with semi-transparent PV glazing could be considered for new EEWs. This is because the PV layers decrease the solar heat gain on the windows, and heat transfer across the glazing can be decreased by the VG [13]. Ghosh et al. [13] estimated the thermal and electrical performance of a hybrid combining STPV with VG, in which a multi-crystalline silicon solar cell was placed on the top surface of the VG sample; with a constant simulated solar radiation level of 1000 $W \cdot m^{-2}$, the system achieved a U-value of 0.8 $W \cdot m^{-2} K^{-1}$. However, the steady-state solar cell temperature under these conditions was approximately 96 ºC. Therefore, a more considerable drop in solar cell power resulted from the elevated temperature in the STPV-VG [13]. This reduction in solar cell power is attributed to the fact that multi-crystalline silicon solar cells have high-temperature coefficients [31]. Further, the same research group conducted a numerical comparison of the uses of STPV samples with and without VG [4]. They concluded that the PV cell temperature difference between these two glazing systems was 24 °C, and confirmed that the STPV hybrid with VG possesses a lower overall heat transfer coefficient [32].

Table 1 summarizes relevant research on the use of semi-transparent PVs with different thermal insulation methods and glazing systems configurations. It is clear that most of these studies utilized crystalline silicon solar cells and arranged them in different locations to accomplish the required window semi-transparency. However, these solar cells are susceptible to temperature because of their higher solar cell temperature coefficient [31]. Nonetheless, all other thin-film solar cell technologies have lower temperature coefficients than do the crystalline silicon-based solar cells [31]. For instance, it is thought that the cell temperature coefficient is -0.45 %/°C for silicon-based solar cells, while it is -0.21 %/°C for cadmium telluride (CdTe) solar cells [31]. Occasionally, the solar cell temperature reached 96 ºC [13], and these high temperatures decrease the efficiency of the crystalline cell. Therefore, the use of CdTe solar cells [31] or dye-sensitized solar cells (DSSCs) [33] is recommended for semi-transparent PV-VG windows.

The novelty of the current study is that, for the first time, the integration of semi-transparent (or 50.8% transparent) CdTe solar cell strings-based glazing to the structured-cored mesh translucent vacuum insulation panel and indium-sealed VG are presented for the modernization of smart windows. This research is intended to compare heating/cooling losses, solar heat gains, induced power, and humidity condensation for the proposed systems. These results contribute to the development of a net-zero-energy building concept as part of the global industrial strategy for climate-change mitigation. Herein are presented experimental and theoretical studies on the thermal and electrical performances of the following six glazing systems: semi-transparent photovoltaic glazing (GPV), VG, translucent vacuum insulation panel (GVIP), semi-transparent PV with VG (VGPV), semi-transparent PV with translucent vacuum insulation panel (VIPPV) and, for comparison, single glazing (SG). These glazing systems are designed, constructed, and tested using a hot box calorimeter with and without simulated indoor solar radiation. This research specifically addresses the knowledge gap regarding the thermal and electrical performances of the TVIP and fabricated VG samples, with and without the integration of the CdTe STPV sample. Tests using infrared cameras were designed to compare the center-of-pane U-values, the transient temperature variations of the inner and outer surfaces of the glazing systems, and the temperature contours.

Further, this work includes the first study on moisture condensation patterns and a comparison of these patterns with those of single-glazed (SG) windows with semi-transparent PV glazing. Furthermore, a detailed 3D finite-volume heat transfer model is developed and validated for all the investigated glazings. The proposed model considers the TVIP core structure design, VG pillars, and edge sealing thermal bridges, thermal vacuum gas conduction, and surface-to-surface radiation, and it includes these factors in the calculations. All these heat transfer mechanisms were thermally coupled to include the interactions between them. The model is validated with the experimental results obtained in this study, and the finite element model results in the literature for VG. The model is used to estimate U-values for the glazing systems considered herein, using ASTM boundary conditions for the winter season.

2. Physical problem

A schematic diagram of the current study is illustrated in Fig. 1. It represents the thermal and electrical performances of glazing systems, and it is suitable for both hot-arid and cold-arid climates. Four distinct designs of energy-efficient glazings are introduced and compared with conventional SG having a thickness of 2.8 mm. In the first design, a glazed photovoltaic (GPV) is introduced. In this GPV, 80 CdTe solar cell strings, with dimensions 1.1 mm × 130 mm, are applied on 3.1 mm thick K-glass. The space between the two CdTe strings is 1 mm. The solar cell strings were electrically connected in parallel using busbars. The total area of the glass pane is 150 mm × 150 mm, and this includes 10 mm of free space along all sides. The area not occupied by the CdTe solar cells, or the transparency, represents 50.8% of the total glass pane area. To protect the CdTe cells, they are embedded in a thin EVA layer with a thickness of 0.6 mm and kept between two glass panes with thicknesses of 3.2 mm. The total thickness of this GPV sample is 7 mm. This type of GPV sample generates electrical power and decreases solar heat gain. However, the temperature rise in the cell structure could increase heat transfer through the glazing to the interior of the building. The VG consists of two low emissive (L-e) coated glass panes having dimensions of 20 mm × 40 mm × 3.1 mm. The two panes are separated by 0.12 mm stainless-steel support pillars arranged in a regular square pattern and spaced at 25 mm. This results in a total VG sample thickness of 6.32 mm. The panel edge seal was accomplished with an indium alloy glass edge seal (width 6 mm) at the periphery of the VG pane. The VGPV is an integration of GPV and VG and offers the advantage of inducing power while reducing thermal transmittance (U-value).

A new TVIP has also been designed and developed. The design differs from that of the conventional VIP, which typically uses an aluminum gas barrier envelope. The current TVIP design uses a structured-core mesh with a transparent gas barrier envelope. This made it possible to resolve the complexity of the edge seal and avoid the consequent construction cost issues usually seen for VGs, typically derived from the use of an edge seal material such as indium. Additionally, this design also avoids the opaque characteristics of conventional VIPs. The proposed TVIPs can be attached as fixed curtains for the windows of existing dwellings by attachment to the existing SGs. The core material is manufactured from a hollow polycarbonate frame encapsulated in a translucent multilayered polymeric envelope to keep the panel element semi-transparent. In addition, an L-e (low-emittance) film is used to decrease the inner radiation exchange. This TVIP is attached to the SG and serves as the reference case for the retrofitting option. The frame dimensions are designed based on the structure model developed in [34], and the dimensions of the frame were δ =1 mm, D = 8 mm, and the total TVIP area is 150 mm ×150 mm. Actual images of the glazing systems investigated herein are shown in the red dashed box of Fig. 1. The dimensions of the transparent gas barrier envelope used in the TVIP, along with its thermal sealing characteristics, are compared with the conventional aluminum gas barrier envelope at the bottom of Fig. 1.

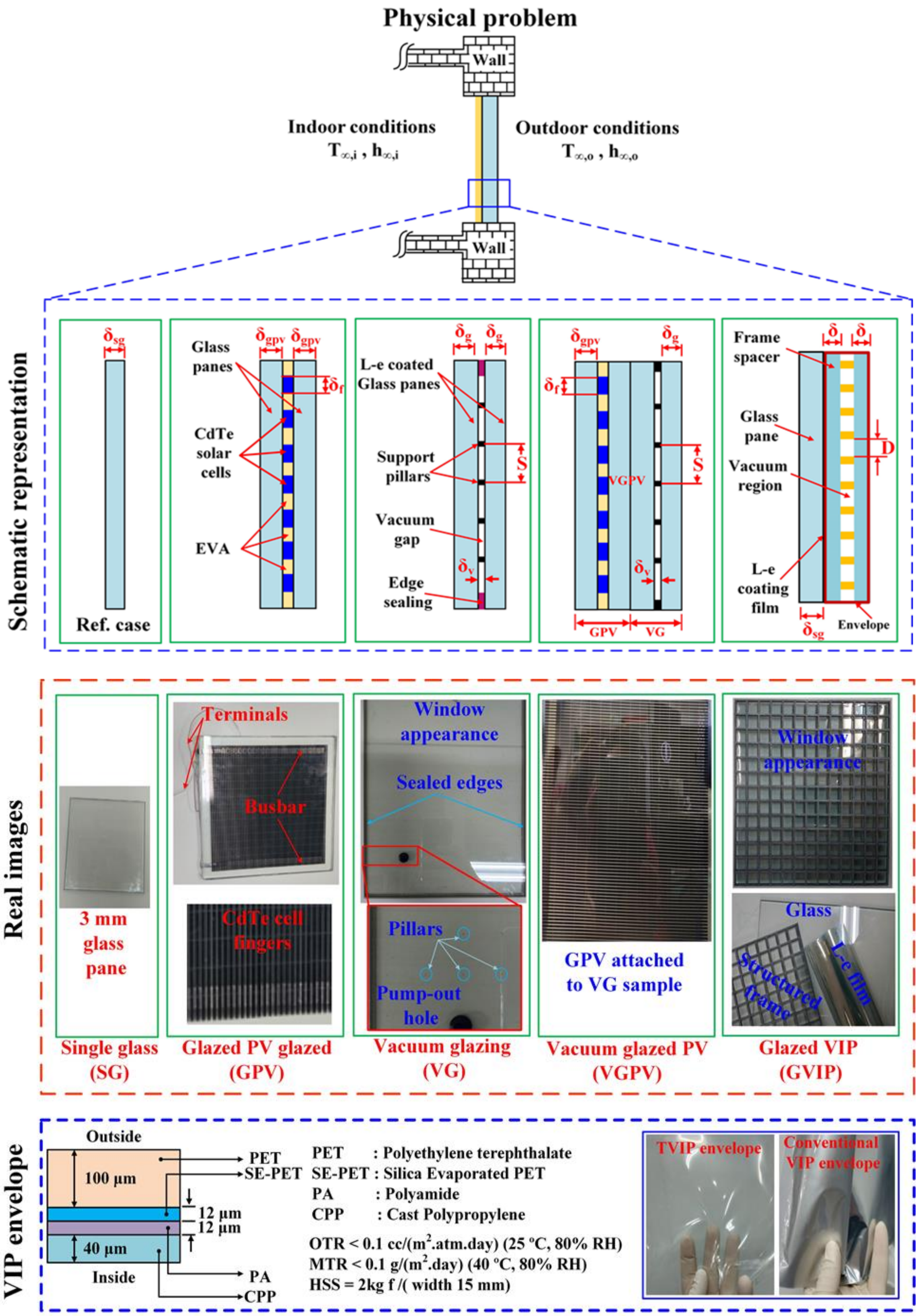

Fig. 1. Schematic diagram illustrating the real field application, schematic representation (top to bottom) of the compared glazing types, real images of the compared glazing types, and characteristics of the TVIP gas barrier envelope.

3. Experimental setups

Three experimental systems are developed in this study. The first experimental system utilizes an apparatus for the evacuation of the VG and TVIP systems, as shown in Fig. 2(a) and Fig. 2(b), respectively. The second experimental system was set up to measure the emissivity of the L-e films using emissometer and thermal conductivity measurements with a heat flow meter (HFM) apparatus, as shown in Fig. 3(a) and Fig. 3(b), respectively. The third experimental system was set up to use hot box calorimetry to compare the thermal performances of the investigated windows, as shown in Fig. 4. The fourth experimental system was set up for comparing solar radiation effects on electrical power output characteristics. The solar radiation is modeled with indoor halogen lamps.

Fig. 2(a) illustrates the evacuation process used for the VG sample. The construction of the VG began with the cleaning of two L-e glass panes using water and then acetone, and this was followed with oven drying at 120 ºC. A pump-out hole with 2 mm diameter was drilled for evacuation, and will ultimately be sealed with an indium sealed glass disk. A 6 mm wide layer of indium was soldered around the periphery on the coated sides of both glass panes. The support pillars were placed on the lower glass pane using a vacuum wand. The upper glass layer was then situated atop the other pane. The sample was heated for 2 hours in the oven to join the two panes of glass. Further, steel-reinforced epoxy was placed around the panel edges to enhance the mechanical stability of the main edge seal. Following that, the sample was placed on a hot plate to heat the pane during evacuation. The evacuation was performed during the heating process, using the vacuum system and vacuum cup shown in Fig. 2(a). After reaching the desired pressure of 0.1 Pa, the pump-out hole was sealed by using a cartridge heater to melt the sealing material fixed inside the vacuum cup. A well-detailed fabrication process with the full dimensions and the mechanism of the vacuum cup was presented in the author’s earlier work [18].

In contrast, the TVIP is constructed from a structured-core frame, L-e film, glass panes with 3 mm thickness, and a gas barrier envelope. All of these items were kept inside the oven at 70 ºC for 24 hours to release outgassing vapor from the structural materials of the VIP. The frame structure and the L-e film were then put inside a three-sided sealed transparent envelope. Three edges of the envelope were sealed using a vacuum sealing machine and a thermal sealing width of 8 mm. The gas barrier envelope was then evacuated with the vacuum sealing machine, as shown in Fig. 2(b), and, after reaching the desired vacuum pressure, the machine automatically sealed the fourth edge. The TVIP sample was then taken out for further experiments. The GVIP sample presented in Fig. 1 is constructed by attaching the TVIP sample manufactured in this section to a 3 mm thick layer of glazing. This attachment technique mimics the retrofitting option for the transparent facades of existing buildings.

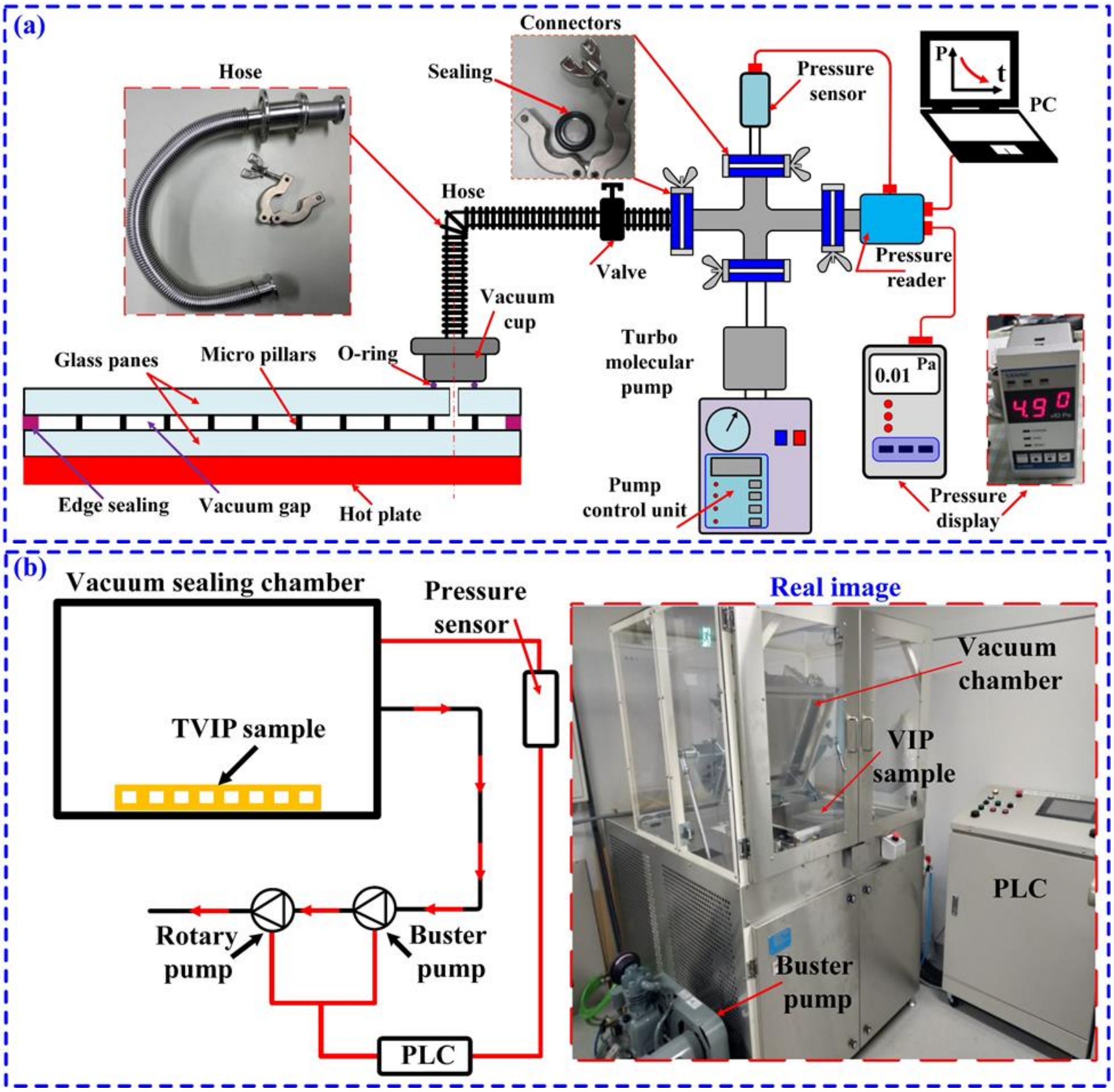

Fig. 2. Detail of the evacuation apparatus involved in the construction of (a) VG sample and (b) TVIP samples.

The experimental setups used for evacuation, pump-out hole sealing, and measurement of the emissivity of the L-e film, as well as that for measurement of thermal conductivity, are illustrated in Fig. 3(a) and Fig. 3(b), respectively. The measurement methods were discussed in [35]. L-e coated glass panes with an emissivity of 0.18 were used for the construction of the VG. The L-e coated face of the glass pane was positioned toward the inner vacuum region, while the L-e coated film used in the TVIP was single face coated. The measured emissivity of the L-e coated side of this film was 0.28.

An HFM was used to measure the thermal conductivities of the samples. The schematic representation and an actual image of the HFM apparatus are contained in Fig. 3(b). This experimental setup allows one to measure the thermal conductivity of a sample with edge widths less than 200 mm. Initially, the sample is inserted into the HFM apparatus. The temperatures of the hot and cold sides of the HFM were kept constant at 35.5 ºC and 10.5 ºC, respectively, for all the tested samples. The HFM has two heat flux sensors on the hot and cold sides, used to measure the heat fluxes on the two faces of the sample after the heat flux reaches a nearly constant value (with deviation set to 2%). The thermal conductivity can be estimated using the flowing relation given in the manufacturer's datasheet:

$$k_{sample} = \left(\frac{q_h + q_c}{2}\right) \times \frac{Sample\ thickness}{\Delta T} \tag{1}$$

where k_{sample} is the pane thermal conductivity in W·m^{-1} K^{-1}, q_h, and q_c are heat fluxes (W·m^{-2}) measured with the two heat flux sensors on the hot and the cold surfaces of the sample, ΔT is the controlled temperature difference for the sample surfaces. The HFM apparatus has the ability to measure these parameters by controlling the temperatures of the hot and cold sides of the sample, along with the sample thickness, with high accuracy.

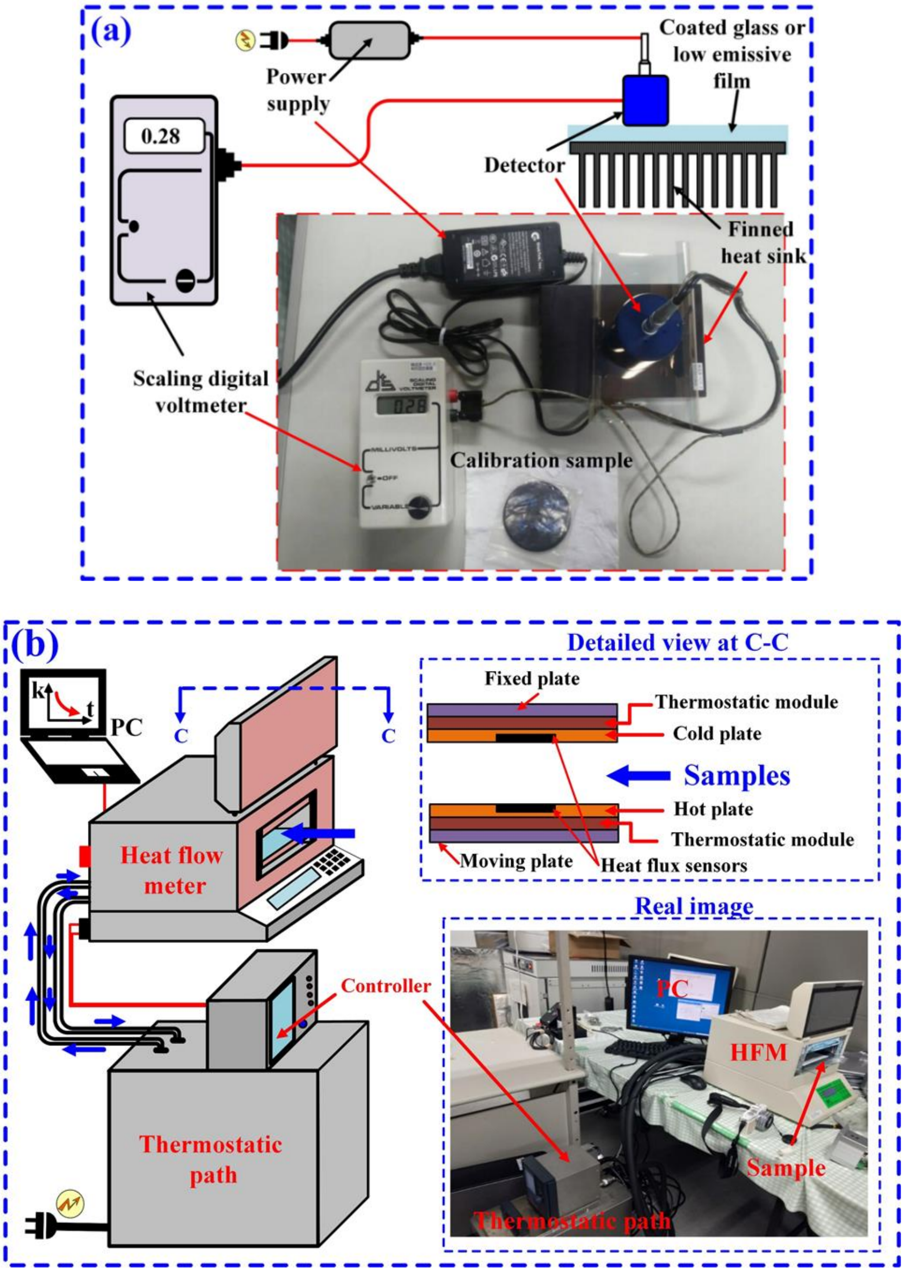

Fig. 3. Experimental components for the measurement of (a) emissivity of the L-e film and (b) thermal conductivity of the six configurations of glazing systems.

Fig. 4 shows the experimental setup used for measuring the insulation performance for each glazing system. The experimental setup consists of a temperature-controlled room, calorimeter, and measuring devices. The temperature-controlled room has a door with an area of 1.15 m × 0.6 m. This door is fabricated from 5 cm thick polystyrene foam insulation. A square area with dimensions 15 cm × 15 cm was cut in the door, and this square area is used to fix the glazing sample. The top of Fig. 4 shows the detailed dimensions of the temperature-controlled room with the square area used for glazing testing. Six calibrated thermocouples were used to measure the temperatures at different locations in the apparatus, as shown in Fig. 4. Two thermocouples at the center of the glazing sample were used to determine the temperature difference across the glazing system by measuring the temperatures of the inner and outer surfaces. Two other thermocouples were used to measure the temperatures of the inner and outer surfaces of the insulation wall, and the final two thermocouples were used to measure the temperatures inside and outside the calorimeter. Further, a thermal infrared camera was used to measure the temperature contours on the outside glass pane of the samples. Finally, the relative humidity of the laboratory was measured using a hygrometer. A photograph of the front surface of the fabricated insulated wall is shown in Fig. 4.

In this experiment, the IR FLIR thermal camera is fixed at a 1-m distance from the front glazing. This camera is used to measure the temperature contours on the front surface of the glazing instantaneously, and the steady-state temperature contour is also captured. The camera is focused to measure the temperature of a square area with dimensions larger than 20 cm × 20 cm; this area includes a 15 cm × 15 cm area for the sample, and the remaining area includes the calorimeter door. This allows us to compare the temperature contours of the sample to those of the foam insulation door. Video and image processing for the recorded video and the captured thermal images was conducted using the FLIR tool provided with the camera.

The samples were tested under two different simulated sets of indoor climatic conditions. The first condition did not include solar irradiation. In this case, the calorimeter inner air temperature was set to −10 °C, while the temperature outside the calorimeter was set to 25 °C without a solar radiation effect (G =0 W·m^{-2}). In this condition, the 25 °C temperature mimics the indoor temperature for thermal comfort, and the −10 ºC temperature models the outdoor weather conditions in a cold region such as in Sapporo, Hokkaido, Japan (43.0618° N, 141.3545° E). This cold condition was used to explore the phenomenon of moisture condensation on the windows in the cold zones.

Another set of simulated climatic conditions was used to measure the electrical characteristics for the GPV sample, alone and with the integration of VG and the TVIP insulation. In this test, the air temperature inside the calorimeter was set to 25 °C, mimicking the temperature used for indoor comfort. The lab was also kept at the same 25 °C temperature while two identical halogen lamps were used, and the solar irradiation level was increased from 200 W·m^{-2} to 1000 W·m^{-2}. The solar radiation meter was located normal to the light and at a distance equal to the distance between the lamp and the glazing sample. Each halogen lamp has an aperture measuring 25 cm × 15 cm. One of the halogen lamps was fixed at a distance of 22 cm from the sample, and the other one was fixed at the same distance from the pyranometer. This pyranometer was used to measure the solar radiation. The halogen lamps were connected to a transformer; this controls the voltage entering the halogen lamps to control the light intensity. A semi-transparent GPV sample was tested as the base sample, and then this sample was integrated with the VG sample and tested under the same conditions. Finally, the GPV sample was attached to the TVIP sample to form a new VIPPV case. Temperatures were measured at different locations on the glazing surfaces, insulation door, and in the air. In addition to this, the instantaneous open-circuit voltage, steady-state short circuit current, steady-state I-V characteristics, and the steady-state PV glazing power were measured with different solar irradiation levels.

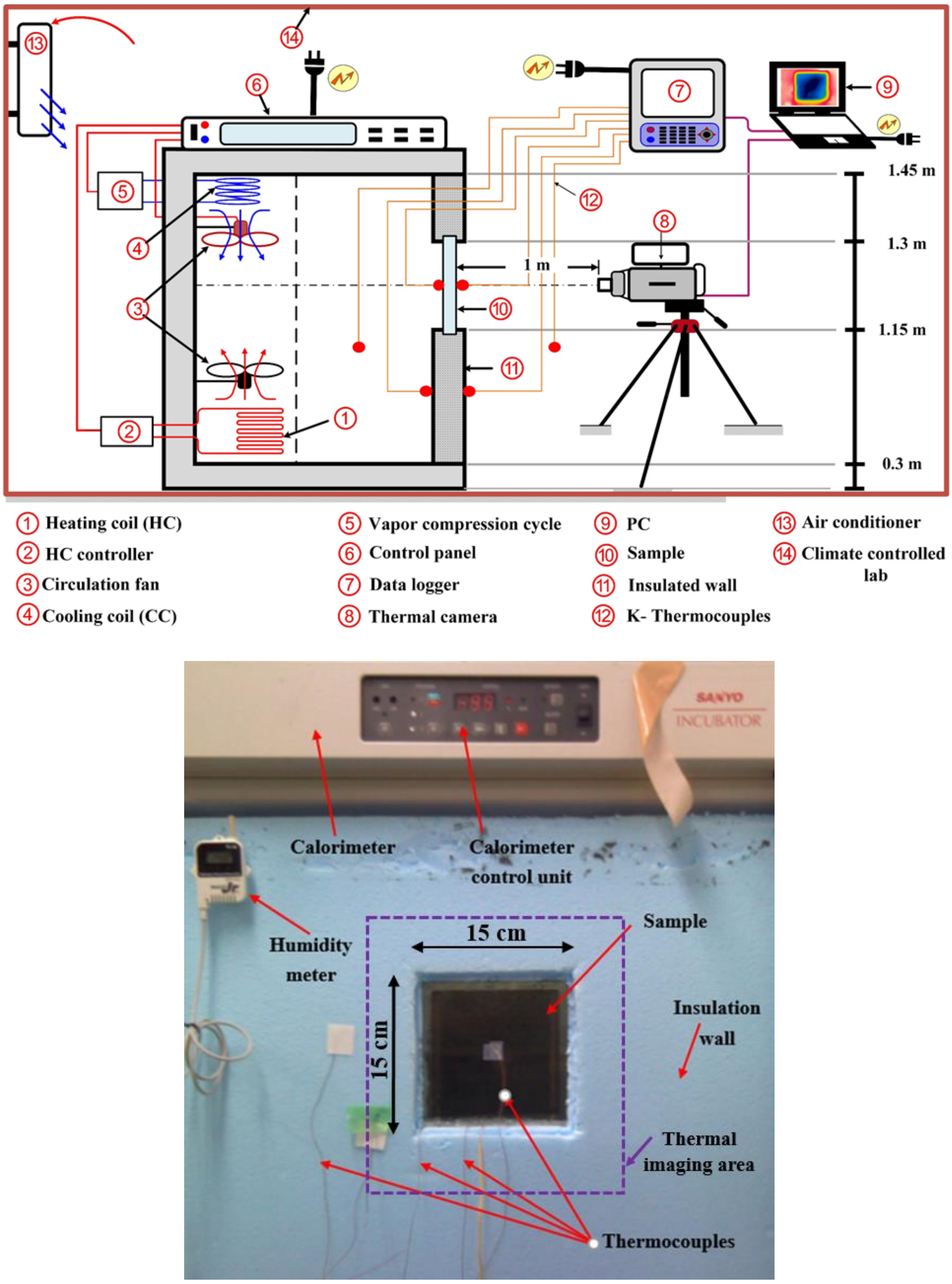

Fig. 4. Experimental setup for the thermal performance analysis of the glazing systems using a hot box calorimeter (top), and the front door of the calorimeter (bottom).

3.1 Experimental procedures

The L-e coated film emissivity was first measured using the experimental setup shown in Fig. 3(a). The VG and the TVIP samples were then designed and constructed using the setups illustrated in Fig. 2(a) and Fig. 2(b), respectively. The thermal conductivities of the samples (described in Fig. 1) and the polystyrene foam insulated calorimeter door were then measured using the HFM apparatus shown in Fig. 3(b). After a series of experiments, it is suggested that a negligible airgap must be considered when measuring the thermal conductivity of the SG and GPV systems. This is because the thermal conductivity of these samples falls outside of the measuring range of the HFM apparatus (0.005 to 0.8 $W{\cdot}m^{-1}\,K^{-1}$). Therefore, to remedy this, the thermal conductivities of the SG and GPV samples were measured by attaching these samples to a 5 cm width polystyrene foam insulation material. By measuring the thermal conductivity of the 5 cm polystyrene foam with and without the SG or GPV samples, the thermal resistances can be obtained. Hence, the thermal conductivities of the SG and GPV samples can be obtained with knowledge of their thicknesses.

The experimental procedures for the setup illustrated in Fig. 4 were begun by adjusting the indoor temperature of the calorimeter and the laboratory room. Then the temperatures at the six locations and the temperature contours were instantaneously measured with the infrared camera and recorded until steady-state conditions were reached. The steady-state condition in this experiment is defined as the condition at which the variations in the temperatures across the samples reach a nearly constant value with a maximum temperature fluctuation of approximately ±2 ºC. This fluctuation is influenced by the calorimeter's on/off controller.

4. Theoretical Modeling Methodology

The main purpose of theoretical modeling is to estimate and validate the U-value of the proposed glazing systems under the standard ASTM boundary conditions for the winter season. The current section presents a detailed discussion of the new modeling method for the VG and TVIP samples, which uses the surface-to-surface radiation model built into the ANSYS Fluent commercial software [36]. For VG and TVIP samples, the heat transfer in the vacuum glazing can occur via four mechanisms. The first is radiation heat exchange between the cold and hot sides of the vacuum region through the vacuum space. The second and third modes are the heat conduction through the skeleton of the core structure of TVIP, the support pillars, and the edge seal of the VG. To improve insulation performance, the exchanges occurring via all these mechanisms must be decreased. With a low-pressure vacuum, the mean-free path between the gas molecules is at least 100 times greater than the vacuum gap size, so gas convection can be disregarded in the calculations [37,38]. The 3D heat conduction equations for all the solid regions were coupled with the surface-to-surface (S2S) radiation model. The S2S model accounts for the radiation heat exchange in the vacuum region. This model is sensitive to the emissivity of the faces in contact with the vacuum region and the view factor. The view factors for all of the surfaces supporting the radiation transfer are calculated based on the detailed geometry dimensions. The current model adopts the following assumptions:

a) The heat transfer between the two glass panes in a vacuum enclosure occurs by radiation between the internal glass surfaces and conduction through the support pillars or the inner frame structure and the edge spacer. The gas conduction effect can be neglected if the internal pressure is less than 0.1 Pa [20]. In this work, the gas thermal conductivity is considered as a function of the pressure, as shown in Eq. (3). However, any residual gas in the cavity will also contribute to heat transfer between the glass panes by gas convection if the pressure is above 10 kPa [37]. The pressure of the fabricated samples was less than 10 kPa. Therefore, the flow continuity and momentum equations were deactivated; i.e., there was assumed to be no gas convection, while the gas conduction is considered as a function of the internal sample pressure in Eq. (3) [19, 37–40].
b) The thickness of the L-e films and the coatings were not considered in conductive heat transfer due to the small width. However, the emissivity of the coatings is considered in radiation exchange and is a dominant factor.
c) The heat conduction through the very thin polymeric envelope used in the TVIP sample, with a thickness of 164 μm (as seen in the bottom of Fig. 1), is neglected.
d) The thermal contact resistances between layers in the glazing structure were not considered.
e) The thermal conductivities of materials were assumed to be isotropic.
f) The thermal conductivity of the vacuum region is a function of the vacuum pressure, the average temperature of the vacuum region, and the pore size [41], as:

$$k_v = \frac{k_o}{1 + \frac{(1.07 \times 10^{-7})T}{l_v P}} \tag{3}$$

where T is the gas temperature in K, l_v is the vacuum layer thickness in m (these are 0.00012 m and 0.003 m for the VG and TVIP systems, respectively), and P is the gas pressure in Pa. In addition, k_o is the air thermal conductivity at room temperature and pressure, which is approximately 0.026 $W \cdot m^{-1} K^{-1}$.

For steady-state and 3D heat conduction with a radiation source, ANSYS FLUENT was used to solve the energy equation as follows [36]:

$$\nabla.(k\,\nabla T) + S = 0 \tag{2}$$

where T is the element temperature, k is the element thermal conductivity, and S is a source term. This last term is added to consider the effect of radiation exchange in vacuum space [36]. In ANSYS, the interfaces between every pair of different layers are thermally coupled. The S2S model governing equations and limitations can be found in the ANSYS theory guide [36], and details were discussed in the author's previous work [35].

The computational domain simulated in this study is depicted in Fig. 5. In addition, the thermal conductivity of each layer in the proposed glazing structures is provided in Table 1.

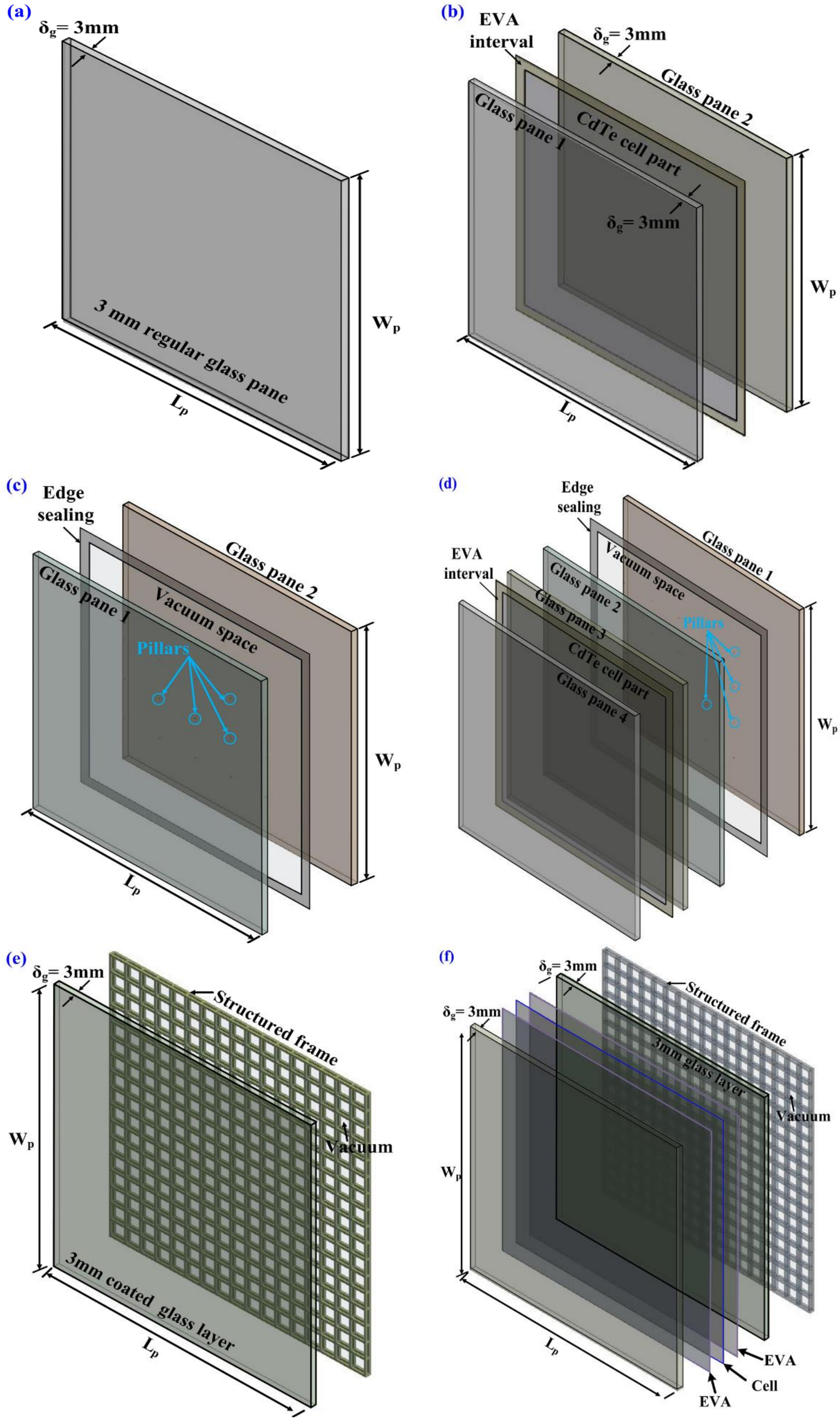

Fig. 5. Axonometric illustration showing the computational domain for: (a) SG, (b) GPV, (c) VG, (d) VGPV, (e) GVIP and (f) VIPPV glazing systems.

Table 2. Thermal conductivities of the layers used in the simulation.

Glazing type	Material	Thermal conductivity	[Ref.]
SG	Glass pane	$0.85\ W{\cdot}m^{-1}\,K^{-1}$	Measured
GPV	Glass pane	$0.85\ W{\cdot}m^{-1}\,K^{-1}$	Measured
	CdTe	$7.5\ W{\cdot}m^{-1}\,K^{-1}$	[42]
	EVA	$0.311\ W{\cdot}m^{-1}\,K^{-1}$	[43]
VG	3 mm coated glass pane	$0.85\ W{\cdot}m^{-1}\,K^{-1}$	Measured
	Pillars	$20\ W{\cdot}m^{-1}\,K^{-1}$	[20]
	Indium sealing	$83.7\ W{\cdot}m^{-1}\,K^{-1}$	[20]
GVIP	3 mm glass pane	$0.85\ W{\cdot}m^{-1}\,K^{-1}$	Measured
	Frame structure	$0.2\ W{\cdot}m^{-1}\,K^{-1}$	[35]

4.1 Boundary conditions

ASTM standards for winter conditions were used in the simulations [20]. In this case, the indoor and outdoor air temperatures are 21.1 °C and −17.8 °C, respectively [18]. The convective heat transfer coefficients on the inside and the outside surfaces of the glazing samples were set to 8.3 and 30 $W{\cdot}m^{-2}\,K^{-1}$, respectively. To include the effect of the L-e coating, the emissivity of the interior glass walls in contact with the vacuum region was defined as 0.18 for VG on both sides of the glass panes and 0.28 for one side of the TVIP (only one sheet of L-e film was used, on the hot side of the TVIP).

Further, the peripheral sides of the glazing were presumed to be adiabatic because of the small thickness of the panes compared to their surface area. Furthermore, thermally coupled boundary conditions were applied at all interfaces. In this case, the temperatures on these interfaces and the heat transfer rates are the same. A mesh independent test was performed to confirm that the results are independent of the number of elements. The number of elements used for the simulation changed according to the computational domain size. A total number of elements of 139876, 979132, 2,964263, 1433729, and 1038336 were used for the SG, GPV, VG, VGPV, and GVIP samples, respectively.

4.2 Numerical methods

The heat flow equations, including those for continuity, momenta, and energy equations, were implemented in Fluent. However, in the current study, the flow equations were deactivated because the effects of gas convection are neglected [16,44]. The energy equations for radiation of the solid regions and the vacuum regions were solved simultaneously. The radiosity estimation is achieved based on the estimated view factors. The process was continued until the residuals in the radiosity and the energy equation reached 10^{-6} and 10^{-13}, respectively.

4.3 Model validation

The current model was validated using two sets of data. First, the predicted temperature differences across the samples were compared with the experimental temperature differences measured with the setup in Fig. 4. Knowing the experimental temperature difference across the sample, the measured thermal conductivity of the samples, and the air temperatures inside and outside the calorimeter, the heat flux through the sample and the inner and outer convection heat transfer coefficients were estimated from the following equations:

$$q'' = k_{sample} \times \frac{(T_{g,o} - T_{g,in})}{\delta_{sample}} \qquad (4)$$

$$h_{\infty,in} = \frac{q''}{(T_{g,in} - T_{\infty,in})} \qquad (5)$$

$$h_{\infty,o} = \frac{q''}{(T_{\infty,o} - T_{g,o})} \qquad (6)$$

where q'', $h_{\infty,in}$, $h_{\infty,o}$, $T_{g,in}$, $T_{g,o}$, $T_{\infty,in}$, and $T_{\infty,o}$ are the transmitted heat flux (W·m^{-2}), convection heat transfer coefficients inside and outside the calorimeter (W·m^{-2} K^{-1}), inside and outside glazing surface temperatures (ºC), and the air temperatures inside and outside the calorimeter (ºC), respectively. These parameters were measured with experiments involving steady-state conditions and used as boundary conditions for the numerical model, and the parameters are displayed in Table 2. To validate the numerical model, the model was simulated with convection boundary conditions for the inner and outer sides of $h_{\infty,in}$ and $h_{\infty,o}$ with the corresponding free stream temperatures $T_{\infty,in}$ and $T_{\infty,o}$, respectively. In the validation step, the vacuum pressures in the VG and TVIP samples were 0.1 and 1 Pa, respectively.

Table 3. Steady-state experimental parameters used in the validation step (the shaded columns were used in place of ASTM parameters as boundary conditions for the validation step).

Sample	$T_{g,in}$ **(ºC)**	$T_{g,o}$ **(ºC)**	$T_{\infty,in}$ **(ºC)**	$T_{\infty,o}$ **(ºC)**	k_{sample} **(W·m^{-1} K^{-1})**	δ_{sample} **(mm)**	q'' **(W·m^{-2})**	$h_{\infty,in}$ **(W·m^{-2} K^{-1})**	$h_{\infty,o}$ **(W·m^{-2} K^{-1})**
SG	5.48	7.88	-8.65	26.40	0.85	2.8	711.5	50.3	38.4
GPV	3.60	7.19	-8.27	25.72	0.337	7.0	172.48	14.5	9.3
VG	-6.99	21.29	-9.08	25.46	0.008	6.4	37.63	18.0	9.0
VGPV	-6.29	20.76	-8.81	25.52	0.018	13.4	36.56	14.5	7.7
GVIP	-2.76	17.01	-9.55	25.87	0.026	6.5	79.37	11.7	9.0

Fig. 6 compares the simulation results with the experimental steady-state results for the heat flux at the center of the glazing systems. It is evident that the model accurately predicts the thermal transmittance performance of the examined glazing systems with a maximum relative error in the heat flux of 8.5% for the VGPV sample. This error may have arisen from neglecting the contact resistance resulting from attaching the GPV sample to the VG system.

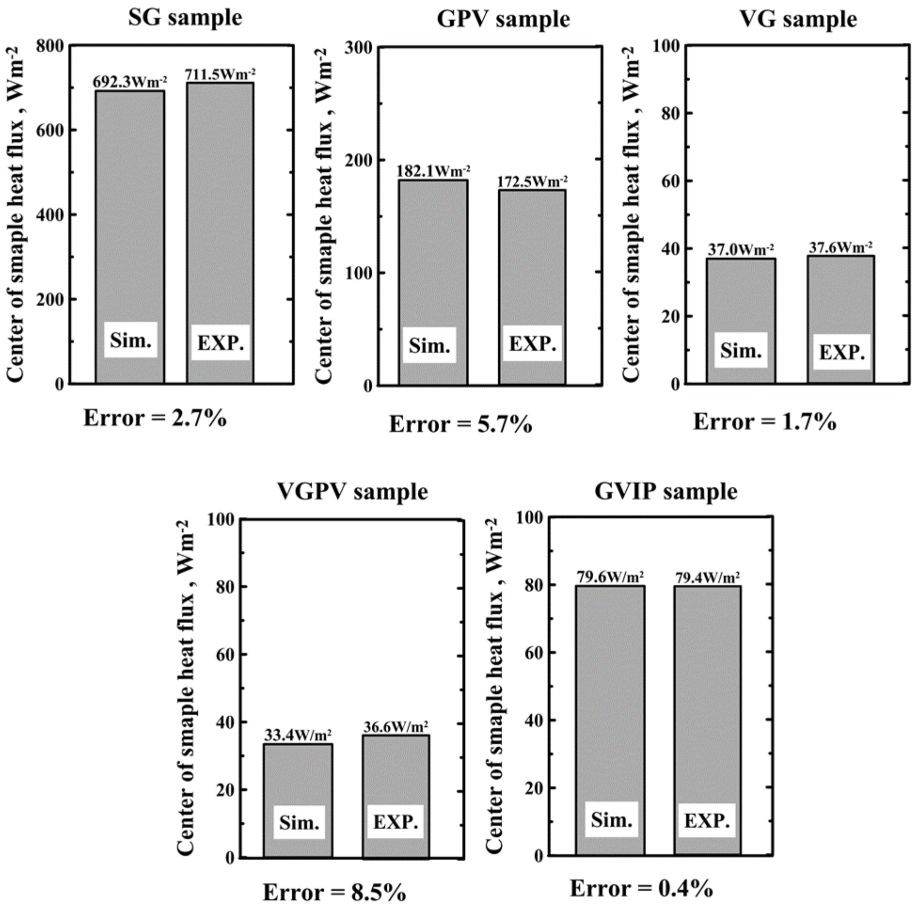

Fig. 6. Comparison of the predicted sample center heat flux with the measured value for the indicated samples.

To validate further the current numerical model, the predicted results for the VG sample were compared to the results of Fang et al. [20]. They used a finite element model to estimate the U-value and temperature distributions over the cold and hot sides of a VG panel with dimensions 40 cm × 40 cm. The VG in Fang et al. [20] is similar to that used in the current work, with stainless steel pillars having a diameter of 0.3 mm and a height of 0.12 mm. Two L-e coated glass panes with 4 mm thickness and emissivity of 0.18 are used. The VG sample was also sealed with indium edge sealing material. In this section only, a quarter of the VG sample is simulated to save computational time, following Fang et al. [20]. Furthermore, the temperature distributions on the cold and the hot sides of the VG are compared with [20]. The comparisons were discussed in the author's earlier work [45], and they showed excellent agreement.

5. Results and discussion

This section is divided into three main subsections. Section 5.1 describes the experimental results for the thermal insulation tests of the proposed glazing systems (without solar radiation). Section 5.2 presents results for the electrical and thermal performances of the proposed glazing systems with simulated indoor solar radiation levels ranging from 200 $W{\cdot}m^{-2}$ to 1000 $W{\cdot}m^{-2}$. Section 5.3 presents a numerical comparison of the insulation performances for the proposed glazing systems operating under ASTM boundary conditions.

5.1. Thermal performances without solar radiation

The experimental transient and steady-state thermal performances of the proposed glazing systems are presented below. To mimic the outdoor cold conditions, the air temperature inside the calorimeter was set to −10 ºC, and, to represent the indoor environment of the room, the air temperature in the lab was set to 25 ºC using the air conditioning system. The instantaneous air temperature inside the calorimeter $T_{\infty,in}$ the air temperature outside the calorimeter $T_{\infty,o}$ the glazing temperature on the inside and the outside surfaces, $T_{g,in}$ and $T_{g,o}$ respectively, and the temperatures of the foam insulated door on the inside and the outside surfaces, $T_{ins,in}$ and $T_{ins,o}$, were measured. Additionally, the very low inner calorimeter temperature led to moisture condensation on the outside surface of the glazing. This degrades the transparency and causes cracking of wooden window frames. Therefore, the moisture condensation pattern is compared to these glazing systems, as is the thermal imaging pattern.

5.1.1 Transient thermal analysis

Fig. 7 shows the instantaneous variations in $T_{\infty,in}$, $T_{\infty,o}$, $T_{g,in}$, $T_{g,o}$, $T_{ins,in}$ and $T_{ins,o}$, along with the moisture condensation patterns. All of these temperatures started at approximately the lab temperature (25 ºC) and decreased with time, and this decrease was caused by the operation of the calorimeter. Fig. 7(a) displays the variations of these temperatures for the SG. The temperature $T_{\infty,in}$ is seen to decreases with time until it reaches −10 ºC and fluctuations commence. This is caused by the on/off controller of the calorimeter. This fluctuation also influences the measured $T_{ins,in}$, which exhibits the same pattern. This temperature fluctuation also influences the inner and outer glass temperatures, $T_{g,in}$ and $T_{g,o}$. For the SG sample, it is evident that the temperature difference across the sample at steady state is only approximately 2.3 ºC; this means that, for the SG sample with a thermal conductivity of 0.85 $W \cdot m^{-1} K^{-1}$ and thickness of 2.8 mm, the total heat flux is approximately 711 $W \cdot m^{-2}$. In addition, the measured values for both $T_{g,in}$ and $T_{g,o}$ are lower than the dew point temperature of the air in the lab at $T_{\infty,o}$. This causes more moisture condensation over the outer surface of the pane, and this decreases visibility through the glazing. Although both $T_{g,in}$ and $T_{g,o}$ were smaller, no moisture condensation was observed on the surface with a temperature $T_{g,in}$. This is because the inner air temperature $T_{\infty,in}$ decreases the dew point of the air inside the calorimeter. Further, the temperature difference across the foam insulated wall is approximately 30.7 ºC, resulting in a smaller heat flux loss of 25.7 $W \cdot m^{-2}$ (from $T_{\infty,in}$ to $T_{\infty,o}$) through the 5 cm wall. Therefore, the heat flux through the SG is approximately 27 times the heat loss through the foam wall.

Fig. 7(b) shows the results obtained with the GPV sample, using the same temperatures and testing conditions as above. It is noticed that a similar trend was exhibited, except for a more significant temperature difference across the glazing sample. This is because the total thermal conductivity of this sample is 0.3 W·m^{-1} K$^{-1,}$ with a total thickness of 6.3 mm. This smaller value for thermal conductivity, together with a larger thickness, increases the glazing thermal resistance. Therefore, the heat flux transfer through this sample is only 172.8 W·m^{-2}, while it remains constant for the foam wall. Also, it is observed that the outer temperature of the GPV sample, $T_{g,o}$, is still less than the laboratory dew point temperature. Therefore, moisture condensation occurs, as seen in the right-hand side of Fig. 7(b).

Fig. 7(c) shows the results from testing of the VG sample. The temperature difference across the glazing became very large, reaching approximately 28.8 ºC. This is due to a significantly smaller steady-state heat flux transfer through the glazing, 37.6 W·m^{-2}, which is only 1.5 times higher than the heat transfer flux through the foam insulation wall. The measured $T_{g,o}$ is slightly affected by the temperature fluctuation inside the calorimeter. Furthermore, the outside surface temperature of the pane, $T_{g,o}$, rises above the dew point temperature of the laboratory air. This prevents moisture condensation on the surfaces of the glazing system.

To consider the further enhancement of the insulation performance and electrical power generation by the glazing, the VGPV sample was tested, and the results are presented in Fig. 7(d). Trends similar to those for the VG sample were observed, with a significant temperature difference across the sample (27 ºC) and a glazing heat flux of 36 W·m^{-2} with a sample thickness of 13.3 mm. Moisture condensation was not observed. Fig. 7(e) shows the measured temperatures for the GVIP sample. In this sample, the TVIP was fabricated with a vacuum pressure of 0.25 Pa and attached to a 2.8 mm thick glass layer. It is found that the temperature difference across the two sides of the window is approximately 19.7 ºC. This results in a steady-state heat flux of 79.3 W·m^{-2}, which is roughly 3 times higher than is the heat flux through the foam wall. In addition, slight condensation is observed on the surface of the glazing. In comparison, moisture condensation starts after 20 min, 25 min, and 45 min for the SG, GPV, and VIPG glazing systems, respectively. From visual inspection, it is clear that the highest condensation rate occurs with SG, followed by GPV, and then the GVIP sample.

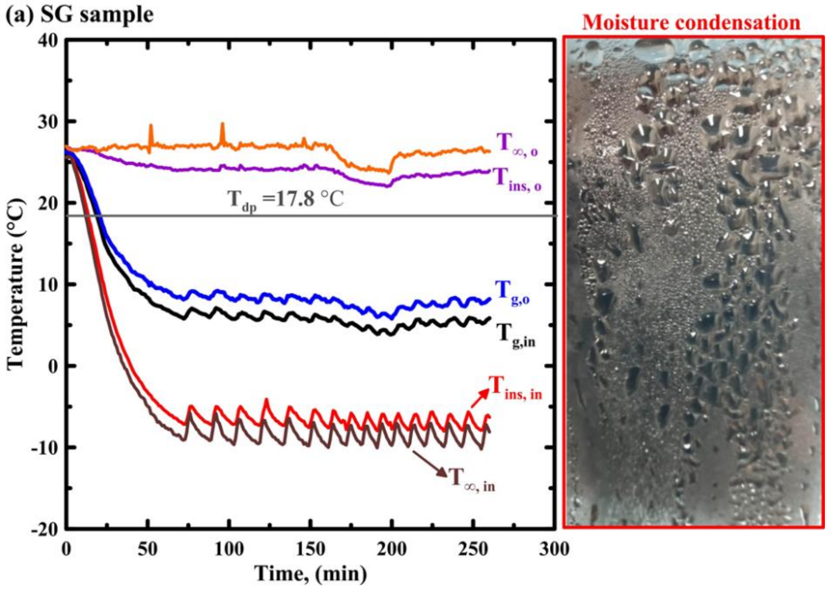
(a) SG sample
Moisture condensation
Temperature (°C)
Time, (min)
T∞, o
Tins, o
Tdp =17.8 °C
Tg,o
Tg,in
Tins, in
T∞, in

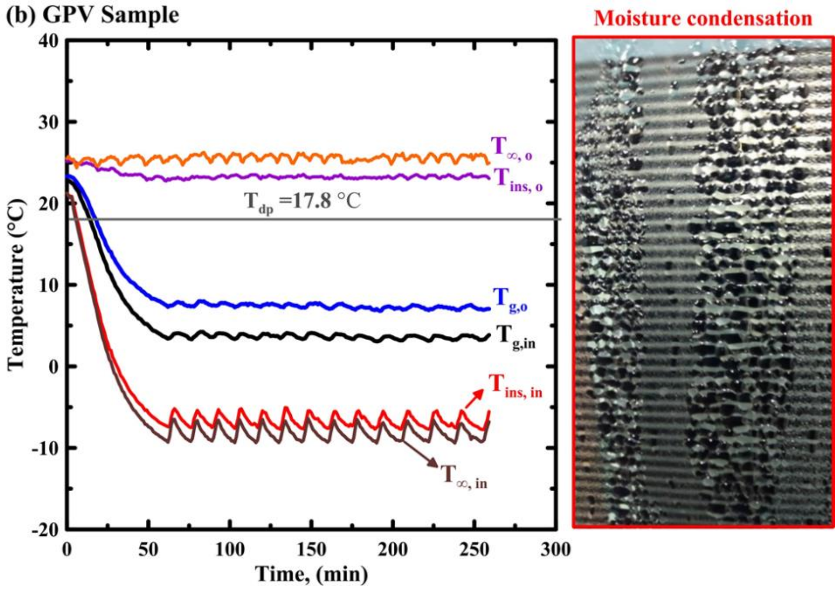
(b) GPV Sample
Moisture condensation
Temperature (°C)
Time, (min)
T∞, o
Tins, o
Tdp =17.8 °C
Tg,o
Tg,in
Tins, in
T∞, in

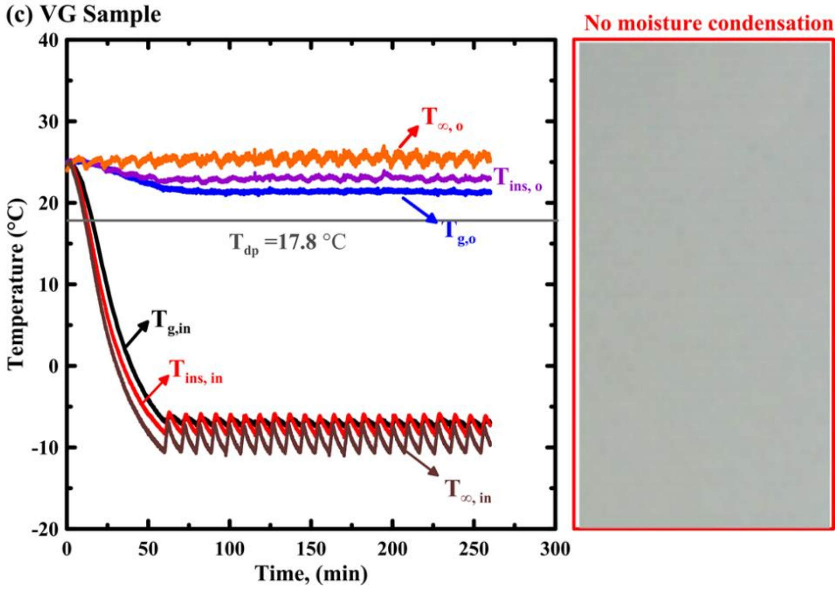
(c) VG Sample
No moisture condensation
Temperature (°C)
Time, (min)
T∞, o
Tins, o
Tg,o
Tdp =17.8 °C
Tg,in
Tins, in
T∞, in

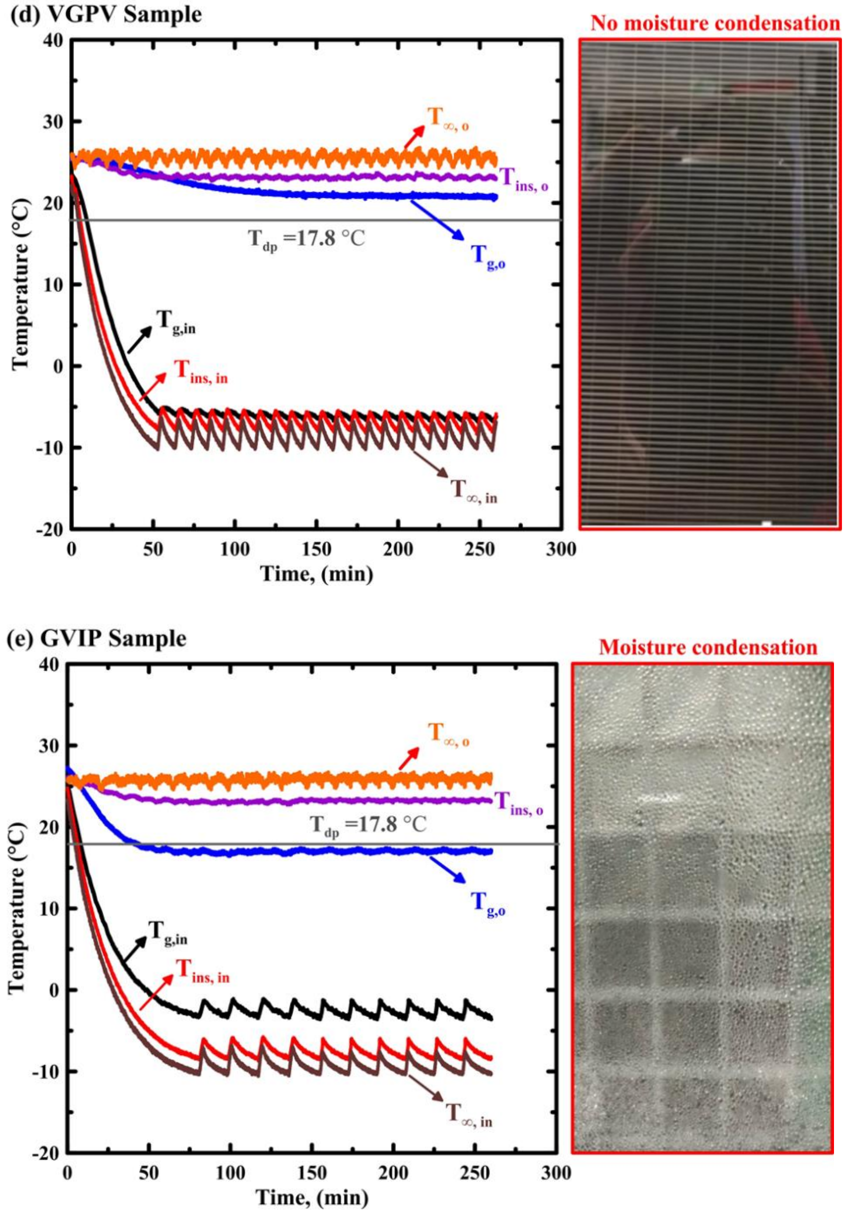

Fig. 7. Transient variations of measured temperatures with condensation pattern for (a) SG, (b) GPV, (c) VG, (d) VGPV, and (e) GVIP glazing systems.

5.1.2 Steady-state thermal analysis

Fig. 8 shows the measured temperature contours for the proposed glazing systems on the outside surfaces, with temperature $T_{g,o}$. The instantaneous temperature contour is recorded with the thermal camera operating at the rate of 15 frames/s. The steady temperature contour is extracted from the recorded video for 250 min of the experiment for all the proposed glazing systems. The contours displayed in Fig. 8 are for an area beginning 2.5 cm from the insulation wall on all sides. The purpose of this experiment is to clarify the insulation performance of the glazing systems as compared with that of the 5 cm thick opaque insulation wall. Therefore, the temperature contours in this section cover an area of 20 cm × 20 cm, and the glazing system coordinates start at $0 \leq x \leq 15$ cm and $0 \leq y \leq 15$ cm.

Temperature contours were recorded and processed using FLIR software provided with the IR thermal camera. Further, two lines A-a and B-a were drawn at the mid-height and mid-width points of the images. The temperature distributions along these two lines were extracted from the thermal images using the FLIR tool and are compared for all cases on the right-hand sides of Fig. 8.

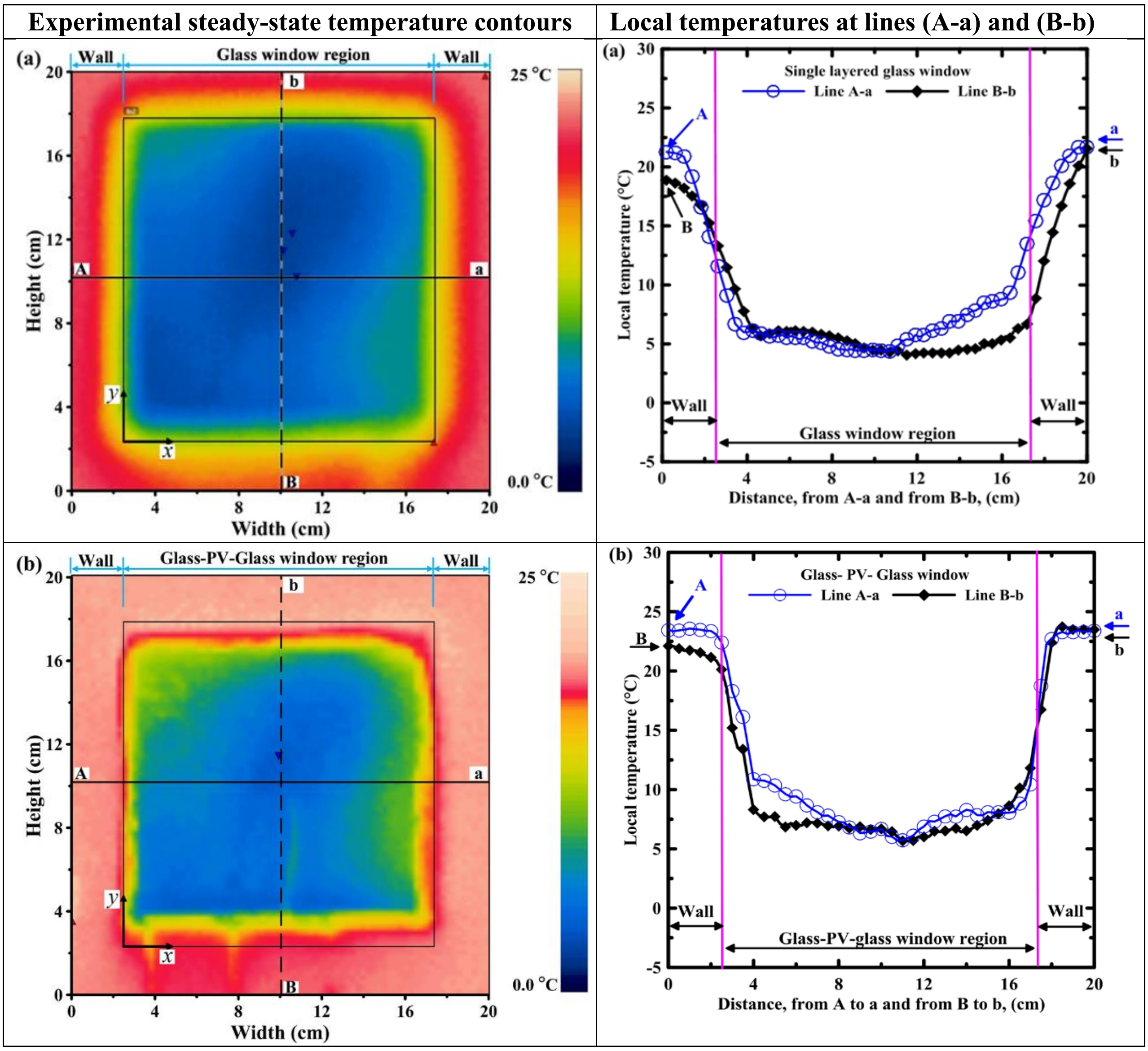

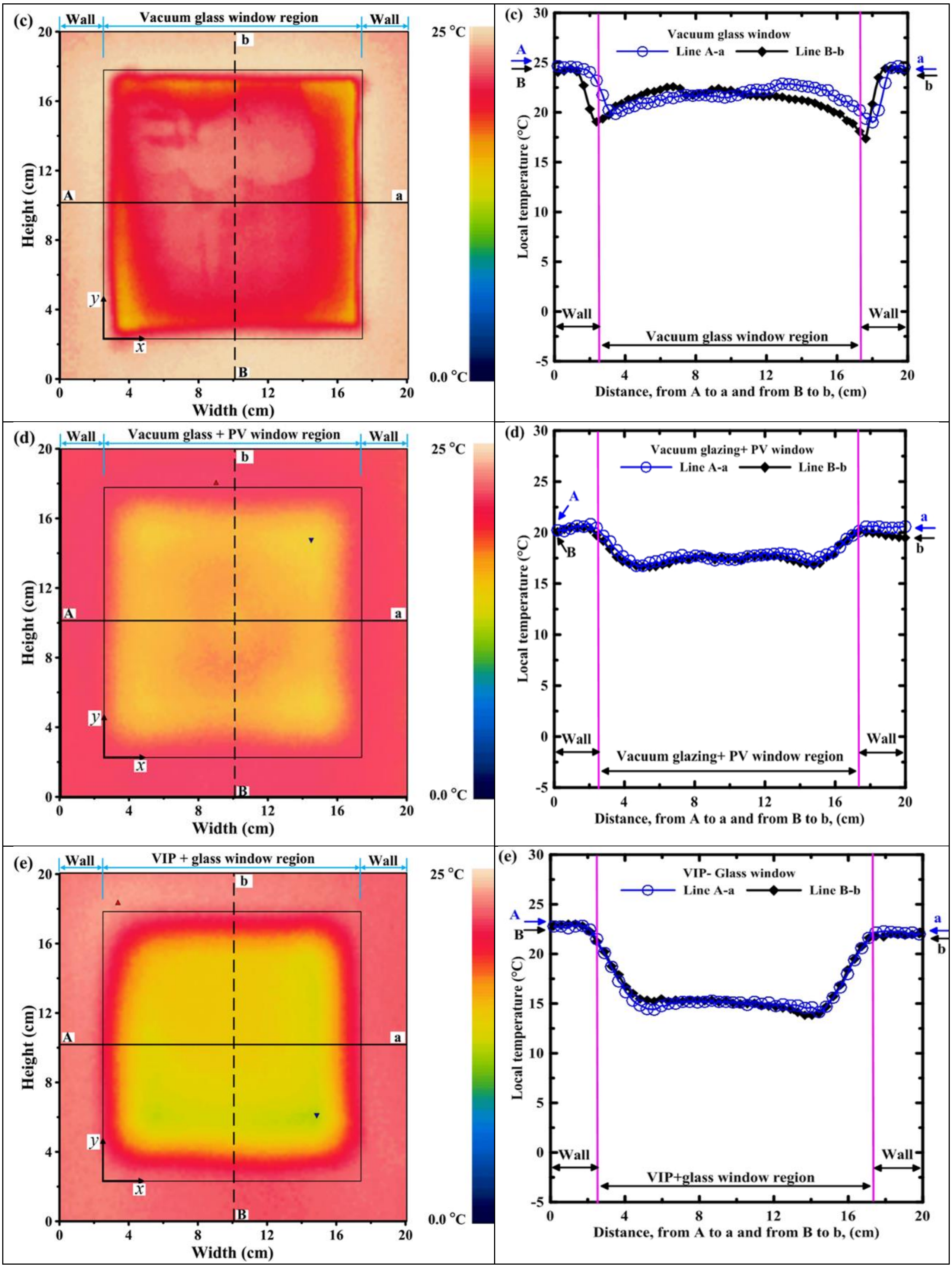

Fig. 8. Measured temperature contours (left) and temperature distributions over the lines A-a and B-b (right) for the samples (a) SG, (b) GPV, (c) VG, (d) VGPV, and (e) GVIP.

From Fig. 8, it is clear that the minimum temperature is typically located in the glazing region. This means that the insulation capability of the glazing is less than that of the 5 cm insulation wall. However, the minimum temperature contours were measured for SG, followed by GPV, and then GVIP. To analyze Fig. 8(a), the local temperatures at the insulated wall are approximately 25 ºC at points x = -2.5 cm and x = 20 cm, while the minimum glazing temperature, approximately 5 ºC, is achieved at the center of the glazing area.

Fig. 8 shows that, on line, A-a, the point A is located at x = -2.5 cm and y = 10 cm while point a is located at x = 20 cm and y=10 cm. The temperature distribution along the line A-a varies with distance, achieving minimum temperatures at the mid-width point and higher temperatures at the ends. The temperatures at points A and a are nearly constant, approximately 25 ºC, for all the cases, while the temperature in the middle of the glazing system changes for every case. For instance, the temperatures at the center of the glazing system (x = 7.5 cm and y =7.5 cm) on line A-a are approximately 5 ºC, 5.2 ºC, 22.5 ºC, 17.5 ºC, and 15 ºC for the SG, GPV, VG, VGPV, and VIPG cases, respectively.

Furthermore, on line B-b the point B is located at x = 10 cm and y = -2.5 cm, while point b is located at x = 10 cm and y=20 cm. The temperature distribution along line B-b varies with distance, achieving minimum temperatures at the mid-width point and higher temperatures at the ends. However, the temperatures at points B and b are not identical, especially in the cases exhibiting moisture condensation. This is because the moisture condensation in the SG (Fig. 7(a)) and GPV (Fig. 7(b)) samples decreases the temperature at point B compared to that at point b. This is not observed in the GVIP case, because the condensation rate is high enough to allow moisture to form on the insulated wall at point B.

5.2 Thermal and electrical performance with different solar radiation levels

In this section, the thermal and electrical performances of semi-transparent photovoltaic glazing systems are investigated, and the effects of solar radiation are considered in the results. Temperatures change as a result of the absorption of solar radiation in the glazing layers. The transient conditions are discussed in section 5.2.1, and then the steady-state results are compared in section 5.2.2.

5.2.1. Transient thermal and electrical analysis

Figs. 9(a), 9(b) and 9(c) show the variations in $T_{\infty,in}$, $T_{\infty,o}$, $T_{g,in}$, $T_{g,o}$, $T_{ins,in}$ and $T_{ins,o}$ as a function of the illumination times for GPV, VGPV, and VIPPV glazing systems, respectively, with a solar radiation level of 1000 W·m^{-2}. Generally, all temperatures increase with increasing illumination time. The highest value is measured for the front glass surface temperature, $T_{g,o}$, and this temperature varies significantly for the different glazing systems. For instance, the measured temperatures ($T_{g,o}$) are approximately 58 ºC, 83 ºC, and 78 ºC for GPV, VGPV, and VIPPV glazing systems, respectively. This results because a fraction of the solar radiation absorbed in the CdTe solar cell is converted to heat. The heat loss from the backside of the solar cell was due to the large thermal resistance caused by the use of VG and VIP with the PV glazing systems. This causes a high cell operating temperature, during the steady-state temperatures, $T_{g,in}$, were approximately 50 ºC, 30 ºC, and 41 ºC for these systems, respectively. The steady state temperature $T_{g,o}$ was reached after illumination periods of 35 min, 75 min, and 50 min for the GPV, VGPV, and VIPPV systems, respectively. The maximum temperature difference across the glazing systems was measured for the VGPV sample, followed by the VIPPV sample, and then the GPV sample. Finally, the measured values for $T_{\infty,in}$, $T_{\infty,o}$, $T_{ins,in}$ and $T_{ins,o}$ were nearly identical for these glazing systems.

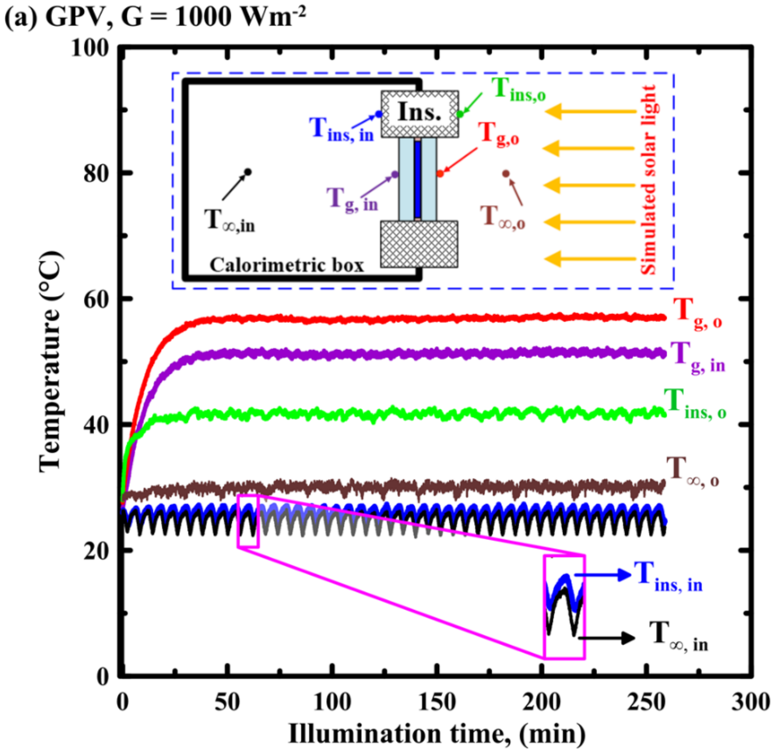

(b) VGPV, G = 1000 Wm-2

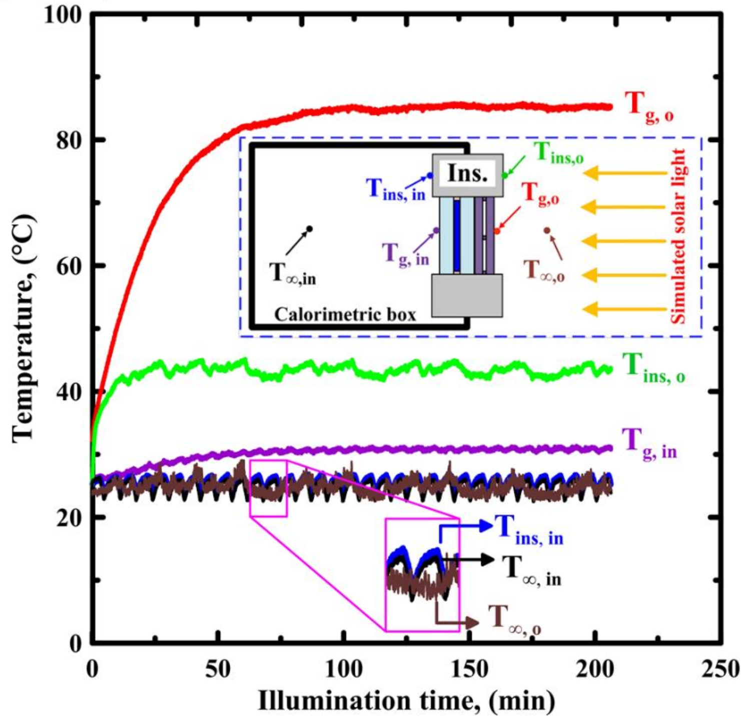

(c) VIPPV, G = 1000 Wm-2

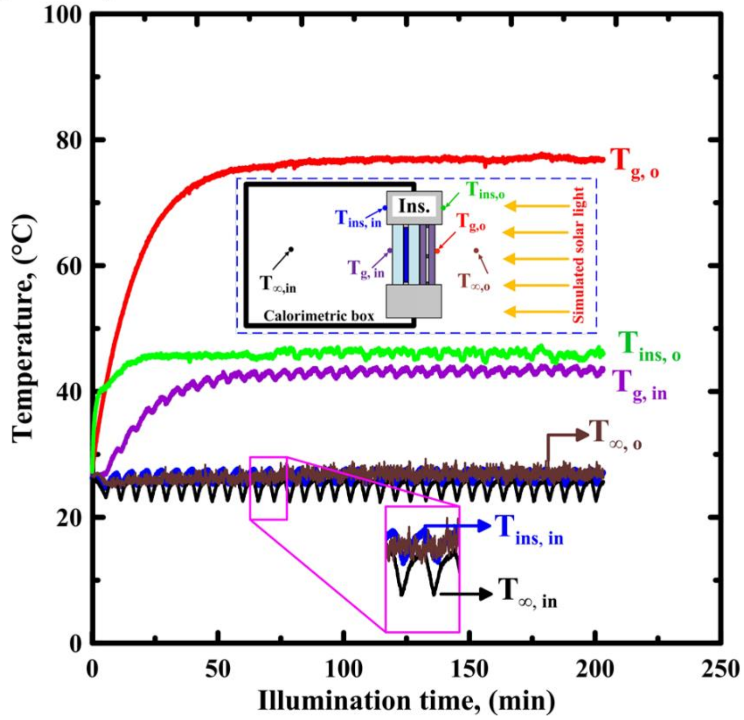

Fig. 9. Instantaneous variations in the measured temperatures $T_{\infty,in}$, $T_{\infty,o}$, $T_{g,in}$, $T_{g,o}$, $T_{ins,in}$ and $T_{ins,o}$ as a function of illumination time for (a) GPV, (b) VGPV, and (c) VIP-PV samples.

The instantaneous temperature differences across the samples and the measured open-circuit voltages are compared in Figs. 10(a) and 10(b), respectively. The temperature difference across the sample is defined as the differences between the measured $T_{g,o}$ and $T_{g,in}$. It is evident that the highest temperature difference is measured for the VGPV sample, followed by the VIPPV sample, and then the GPV sample, with maximum steady-state temperature differences of approximately 55 ºC, 32.5 ºC, and 5 ºC, respectively.

With identical solar radiation levels, increasing the solar cell temperature significantly decreases the open-circuit voltage, and the short circuit current is only slightly affected [13,46]. Fig. 10(b) displays the variations in open circuit voltages versus illumination time with a solar radiation level of 1000 W·m^{-2}. The measured open-circuit voltage, V_{oc}, decreases with illumination time. This is because of the increase in solar cell temperature seen with longer illumination times. After 200 min illumination time, the V_{oc} decreases from 9.75 V to 8.8 V for the GPV sample, from 10 V to 8.3 V for the VIPPV sample, and from 9.75 V to 7.7 V for the VGPV sample. The maximum decrease in the V_{oc} is observed for the VGPV sample, because of the high thermal insulation of the VG. The decrease in V_{oc} for samples using VGPV glazing instead of the conventional GPV sample is 12.5% (with a solar radiation level of 1000 W·m^{-2}), while the heat flux transfer through the VGPV sample was 80 % less than that seen with the GPV sample (as discussed in section 5.1.1).

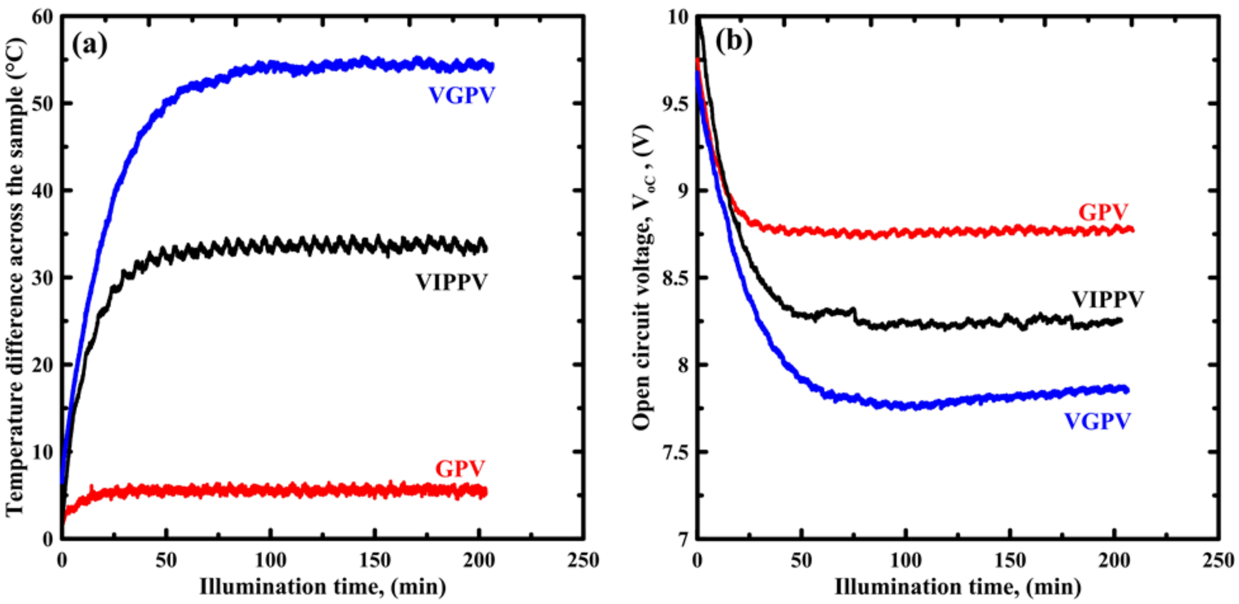

Fig. 10. Instantaneous comparison of (a) temperature difference across the samples and (b) measured open-circuit voltages of the samples with a solar radiation level of 1000 W·m^{-2}.

5.2.2. Steady-state thermal and electrical analysis

The steady-state thermal and electrical performances of PV-based semi-transparent glazings were studied with levels of simulated solar radiation ranging from 200 to 1000 W·m^{-2}. The steady-state temperatures of the sides of the glazing systems, $T_{g,in}$ and $T_{g,o}$, and the steady state temperature difference across them, $T_{g,o}$ - $T_{g,in}$, are presented in Fig. 8. The measured open circuit voltages and short circuit currents with different solar radiation levels are presented in Fig. 9. The measured $T_{g,in}$, $T_{g,o}$ and $T_{g,o}$- $T_{g,in}$ with different simulated solar radiation levels are depicted in Figs. 11(a), 11(b) and 11(c), respectively.

The measured $T_{g,o}$ increases linearly with increasing solar radiation level for all semi-transparent PV glazing systems, as seen in Fig. 11(a). This results from an increase in the solar energy absorbed in the glazing layers, especially for the solar cell wafers, causing higher temperatures. For instance, increasing the solar radiation from 200 W·m^{-2} to 1000 W·m^{-2} increases the temperatures of the front glazing surfaces, $T_{g,o}$, from 32 ºC to 58 ºC, 38 ºC to 78 ºC, and 41 ºC to 87 ºC, for the GPV, VIPPV, and VGPV samples, respectively. In addition, the slope of the line for $T_{g,o}$ versus solar radiation level is higher for the vacuum PV samples, relative to that for the standard GPV sample.

The air temperature inside the calorimeter is considered to be the indoor comfort temperature. This means that the preferred values of $T_{g,in}$ are those closer to 25 °C. The measured temperatures $T_{g,in}$ for the tested samples are illustrated in Fig. 11(b). The maximum $T_{g,in}$ values observed over the entire range of simulated solar radiation levels were those for the standard GPV sample, followed by those for the VIPPV sample, and then by those for the VGPV sample. Additionally, $T_{g,in}$ increases with an increase in solar radiation level. Furthermore, increasing the solar radiation level from 200 W·m^{-2} to 1000 W·m^{-2} led to increases in the measured $T_{g,in}$ from 31 ºC to 51 ºC, 30 ºC to 43 ºC, and 25.2 ºC to 30.5 ºC for the GPV, VIPPV, and VGPV samples, respectively. This indicates that using the VGPV sample results in a very low $T_{g,in}$, closer to that of the typical indoor environment (even at higher solar radiation levels). The maximum differences between $T_{g,in}$ and the indoor setting temperature were around 0.2 ºC and 5.5 ºC for solar radiation levels of 200 W·m^{-2} and 1000 W·m^{-2}, respectively. Finally, the results in Fig. 12(c) show that the difference ($T_{g,o}$- $T_{g,in}$) for the GPV sample increases slightly with solar radiation. This is because of the high thermal conductivity of the GPV sample, which allows heat exchange from both the front and backside of the sample, while, in the VGPV and VIPPV samples, the value of the difference ($T_{g,o}$- $T_{g,in}$) increases significantly with increasing solar radiation level.

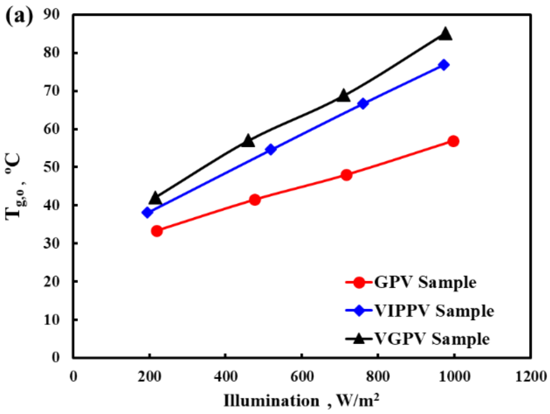

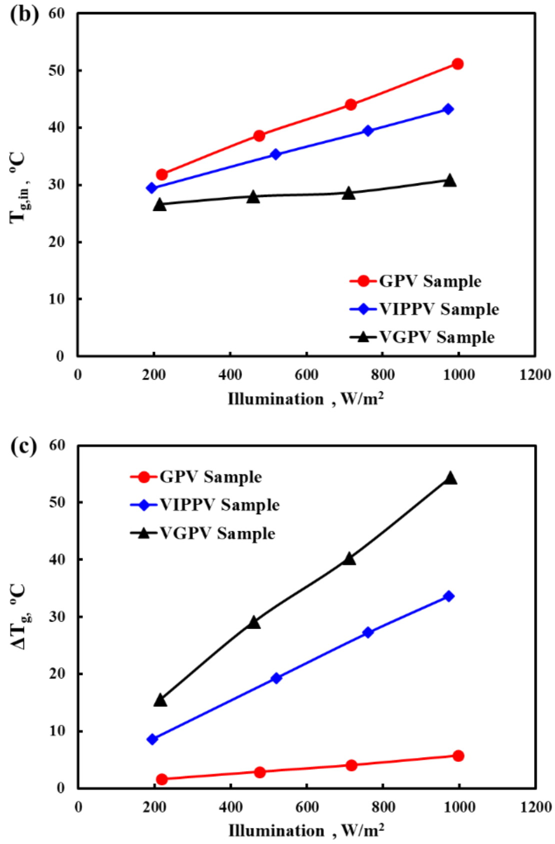

Fig. 11. Influence of simulated solar radiation on the measured (a) $T_{g,o}$ (b) $T_{g,in}$ and (c) $\left(T_{g,o} - T_{g,in}\right)$ for the investigated semi-transparent photovoltaic-based glazing systems.

Fig. 12 shows the electrical performance parameters for the PV-based glazing systems. The results in this figure are displayed in a dimensionless form by comparing them with results for the GPV reference case. For instance, the measured open-circuit voltage and short circuit current for each case is divided by the measured open-circuit voltage and short circuit current for the GPV system, all measured with a solar radiation level of 1000 W·m^{-2}. These ratios are illustrated in Fig. 12(a) and Fig. 12(b), respectively. Furthermore, the fill factors for the samples are also compared in Fig 13(d). The mathematical expressions for these ratios and the fill factor can be written as follows:

$$V_{oc,\ ratio} = \frac{V_{oc,\ sample}}{V_{oc,\ GPV\ at\ 1000Wm^{-2}}} \tag{5}$$

$$I_{sc,\ ratio} = \frac{I_{sc,\ sample}}{I_{sc,\ GPV\ at\ 1000Wm^{-2}}} \tag{6}$$

$$FF = \frac{P_{max,\ sample}}{I_{sc} \times V_{oc}} \tag{7}$$

Fig. 12(a) shows the variation of $V_{oc,\ ratio}$ as a function of the solar radiation levels for the proposed glazing systems, and it is evident that $V_{oc,\ ratio}$ increases with increasing solar radiation levels. In addition, $V_{oc,\ ratio}$ for the GPV sample is the highest among those tested. This is because, for the VGPV and VIPPV samples, an increase in the solar cell temperature results in a decrease in the open-circuit voltage. Increasing the solar radiation level by a factor of five, from 200 W·m^{-2} to 1000 W·m^{-2}, results in increases in the

$V_{oc,\ ratio}$ values of 15%, 12%, and 10 % for the GPV, VGPV, and VIPPV samples, respectively. This shows that the change in solar radiation level has only a small impact on the semi-transparent PV glazing, as is commonly known from the IV characteristics of PV solar cells [47].

Fig. 12(b) shows the variation of $I_{sc,\ ratio}$ as a function of solar radiation levels for the semi-transparent PV samples. It is evident that increasing the illumination intensity causes a proportional increase in the short circuit current ratio, $I_{sc,\ ratio}$, as is also predicted in [48]. This is because increases in the solar radiation level also increase the total energy gained from photon absorption by the solar cell. For example, increasing the illumination level for the GPV sample from 200 W·m^{-2} to 1000 W·m^{-2} increases the $I_{sc,\ ratio}$ to approximately 95%. Further, the VGPV and VIPPV samples exhibited slightly higher $I_{sc,\ ratio}$ values, relative to the GPV sample at the same solar radiation level, because an increase in solar cell temperature slightly increases the short circuit current [47]. Finally, the fill factor (FF) decreases slightly with an increase in the solar radiation level for all of the samples, as displayed in Fig. 8(c); this is in agreement with the results presented in [49]. The highest FF is realized for the GPV sample, and this is because, at the same solar radiation level, the short circuit current is almost the same as that shown in Fig. 8(b). However, the use of the VG and VIP systems attached to the GPV sample increases the temperatures. This results in a decrease in cell output voltage, causing a decrease in the maximum power and consequent decrease in the FF [13].

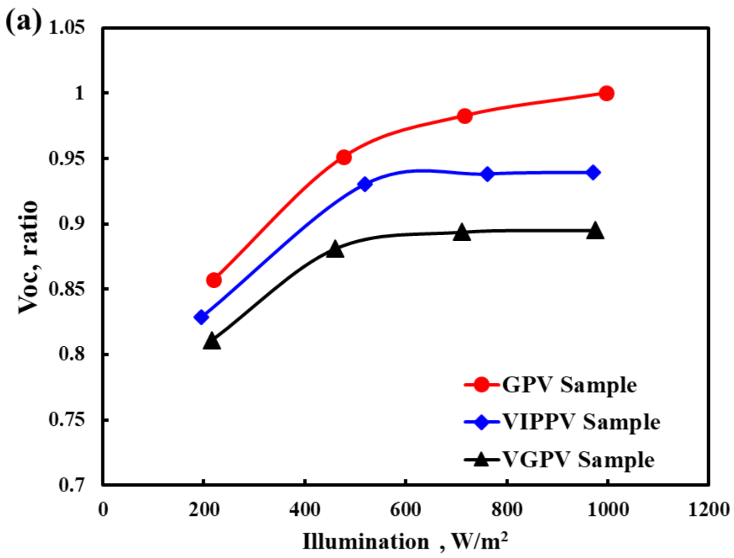

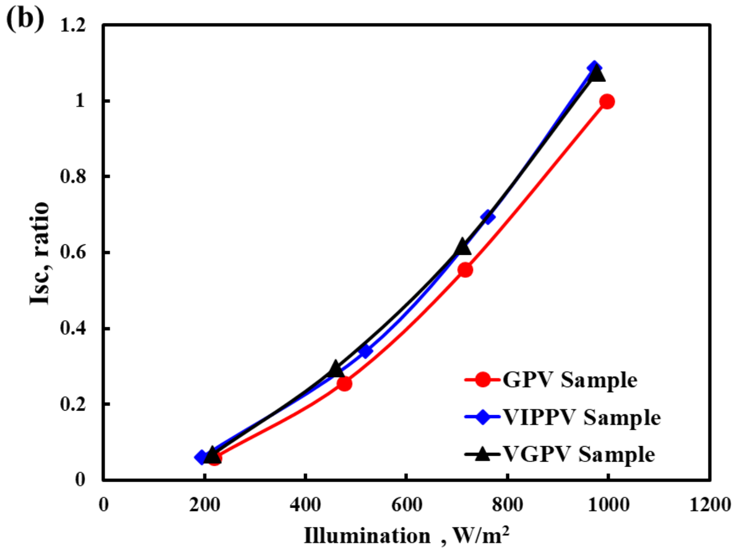

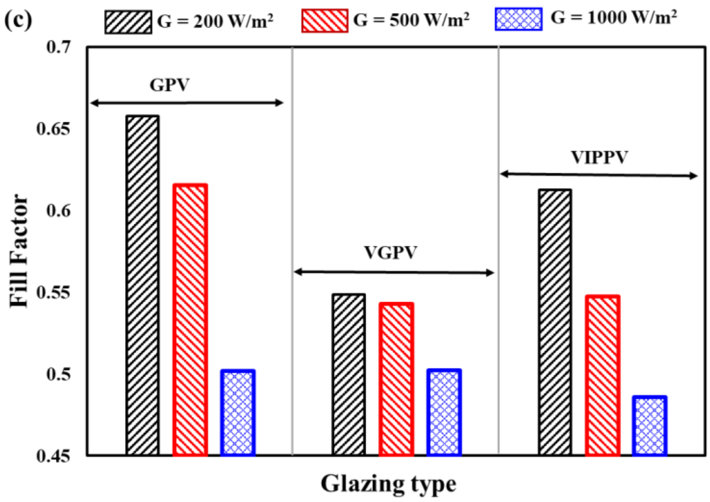

Fig. 12. Steady-state variation of (a) $V_{oc,\ ratio}$, (b) $I_{sc,\ ratio}$, and (c) FF with the indicated simulated solar radiation levels for the semi-transparent photovoltaic-based glazing systems.

5.3. Comparison at ASTM boundary conditions

The U-values for the proposed glazing systems were computationally estimated using the developed numerical model and ASTM boundary conditions. This is important because the cold ASTM conditions cannot be established with the existing calorimeter, which has a minimum attainable air temperature of −10 ºC. Further, even with the lab air conditioner and calorimeter, the inner air temperature and lab air temperature still fluctuate by ±1 ºC and ± 3 ºC, respectively, because of the operation of the controller. Therefore, all the relevant parameters were fixed to ensure a meaningful comparison. The success of this can be confirmed with the modeling approach.

Fig. 13 illustrates the comparison of the predicted contours on the hot side of the glazing systems using the Finite Volume Model (FVM). The hot side panel is selected because it is oriented toward the indoor environment. It was found that the lowest hot side temperature was exhibited by the SG sample, with hot side temperature approximately -8.5 ºC; this was followed by the GPV sample with hot side average temperature of approximately -7.4 ºC, as shown in Fig. 13(a). The VG, VGPV, GVIP, and VIPPV samples exhibited higher average hot side temperatures of approximately 6.8 ºC, 7.1 ºC, 12.4 ºC, and 12.5 ºC, respectively, as shown by the temperature distributions in Figs. 13(b), 13(c), 13(d), and 13(e). The highest temperatures are located at the vacuum regions, and the lowest temperatures occur at the edge sealing and pillars in VG and VGPV samples, and in the frame structure in the GVIP and VIP PV samples. This is because of the thermal bridge effect operating through these highly conductive regions.

Further, the temperatures along two lines on the hot and cold sides of the glazing systems are displayed in Fig. 14 for all proposed glazing systems and these data are compared with those for the SG sample. Figs. 14(a) and 14(b) show that the temperature does not vary with distance in the SG and GPV cases. The higher temperature difference occurs with the GPV sample because it has a thicker structure, and the CdTe layer and two EVA layers have low thermal conductivity.

Figs. 14(c) and 14(d) compare the temperature distributions along the two lines for the VG and VGPV samples, respectively. The hot side temperature is nearly the same for both samples. However, the pillars in the VGPV sample diminished the impact of the cold wall, and this led to a smoother temperature distribution. Additionally, the cold side temperature of the VGPV sample became lower than that of the VG sample. This illustrates the better thermal insulation seen for the VGPV sample. The temperature differences near the edges of the VG and VGPV samples are higher than are the temperature differences at the center of the pane. This is attributed to the thermal bridge operating through the edge seal [50].

Figs. 14(e) and 14(f) compare the temperatures along the same lines for GVIP and VIPPV samples, respectively. The same trends were observed, with a higher temperature difference for the VIPPV sample. For the hot side temperature in both cases, the temperatures at the frame are much lower than are those near the vacuum region, because the thermal conductivity of the frame is higher than is that of the vacuum region.

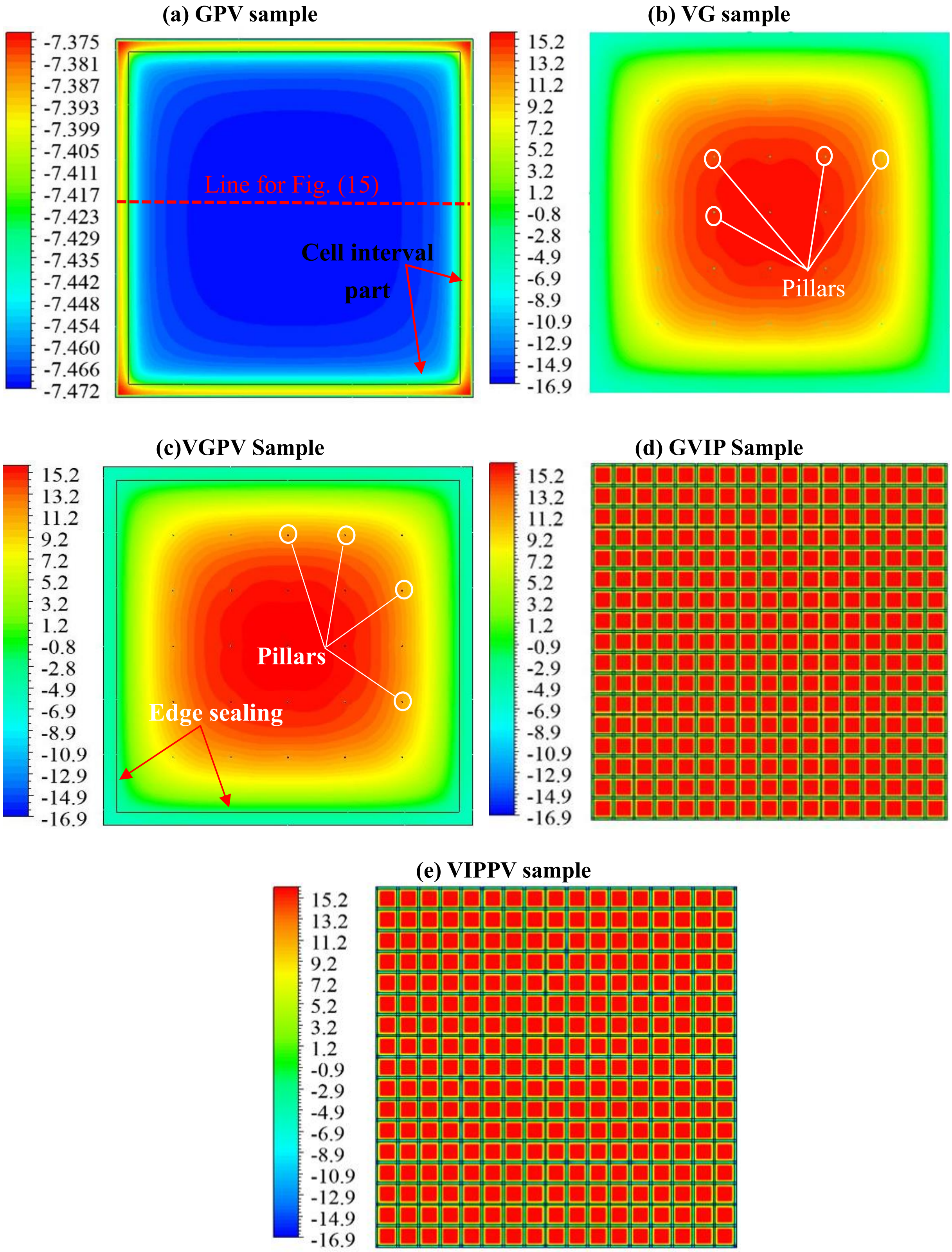

Fig. 13. Variations in hot side temperature contours (ºC) for the proposed glazing systems with ASTM winter boundary conditions.

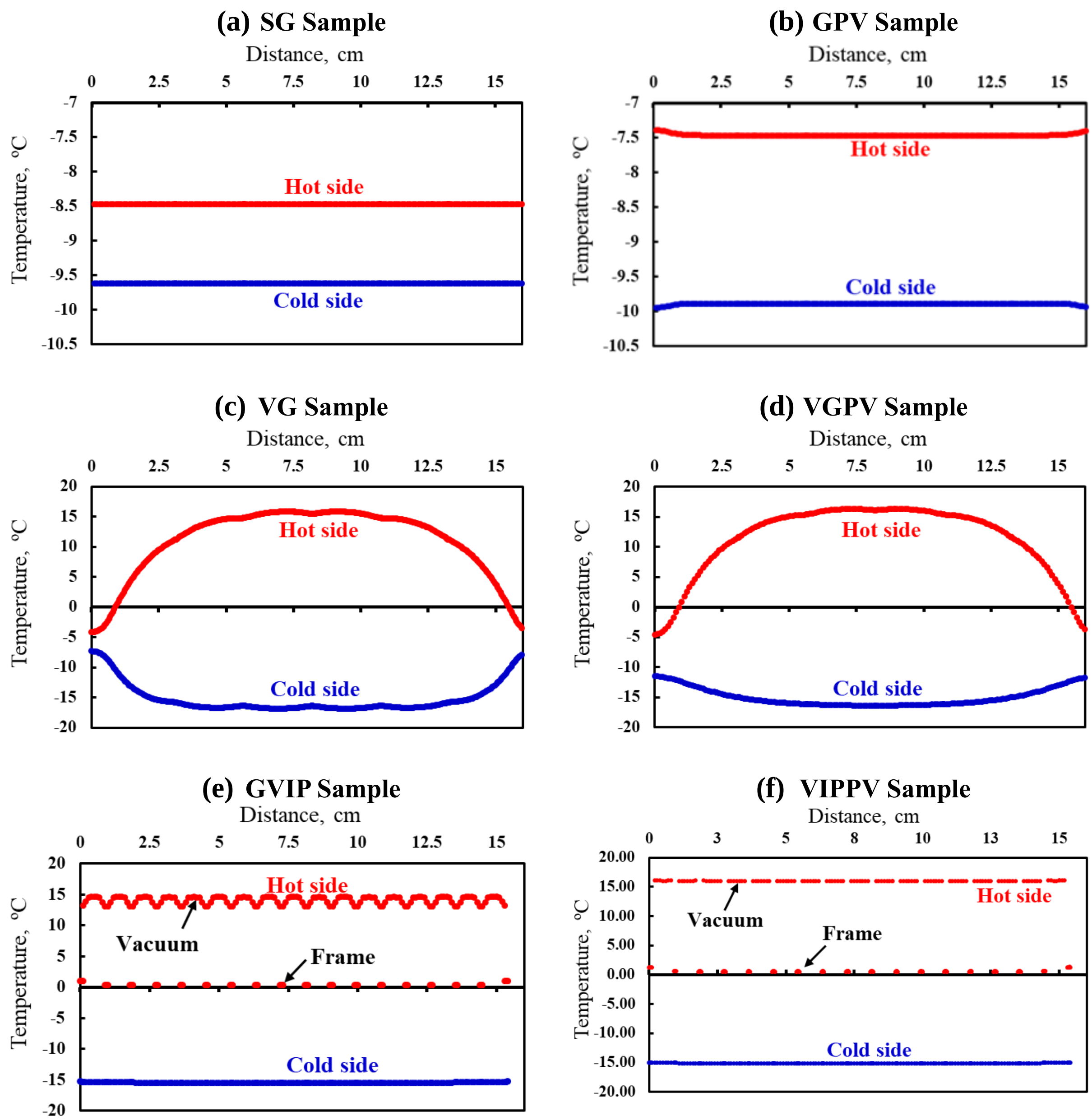

Fig. 14. Local temperature distributions along two lines located on the cold and hot sides at the mid-height points of the (a) SG, (b) GPV, (c) VG, (d) VGPV, (e) GVIP, and (f) VIPPV samples.

The total thermal conductance occurring between the two glass sheets of the VG sample can be written as follows [51]:

$$C_{glass-glass,\ centre-of-glazing} = C_{g-g,\ gas} + C_{g-g,\ radiation} + C_{g-g,\ pillars} \qquad (8)$$

Using the derivation presented in [51], the thermal conductance between the two glazing sheets, not including the edge seal, can be written as:

$$C_{glass-glass,\ centre-of-glazing} = 0.8P + 4\varepsilon_{effective}\,\sigma\,T^{3}_{average,\ glass} + 2k_{glass}a/s^{2} \qquad (9)$$

where P is the internal vacuum pressure in Pa, σ is the Stefan-Boltzmann constant (5.67×10^{-8} W·m^{-2} k^{-4}), $T_{averagre}$ is the average of the temperatures for the hot and the cold sides of the glass panes in Kelvin, k_{glass}

is the glass thermal conductivity ($W \cdot m^{-1} k^{-1}$), a is the pillar diameter in m, and S is the pillar spacing in m. In this study, the values of a and S were 0.4 mm and 2.5 mmm, respectively, and $\varepsilon_{effective}$ is the effective emissivity of the two glass panes and is calculated as follows [20]:

$$\frac{1}{\varepsilon_{effective}} = \frac{1}{\varepsilon_h} + \frac{1}{\varepsilon_c} - 1 \qquad (10)$$

where ε_h and ε_c are the emissivity of the hot and the cold sides of the glass panes, respectively. Those values were 0.18 in the current study. Following the same methodology, the center-of-glazing, air-to-air thermal conductance of the VG sample can be written as follows [51]:

$$\frac{1}{C_{air-air,\ centre-of-glazing}} = \frac{1}{h_{\infty,i}} + \frac{1}{C_{glass-glass,\ centre-of-glazing}} + \frac{1}{h_{\infty,o}} \quad (11)$$

Equations (8) – (11) were used to estimate the value of $C_{air-air,centre-of-glazing}$ for the VG and VGPV samples without considering the effects of edge sealing, and this term can also be considered as the center-of-pane U-value. The temperatures of the hot and the cold sides of the glass panes were estimated from the numerical model, and these values were used in equations (8) – (11) to estimate the center-of-pane U-value. Fig. 15 shows a comparison of U-values for all samples, using ASTM winter season boundary conditions and a vacuum pressure of 0.1 Pa. The VG and the VGPV samples exhibited the lowest center-of-pane U-values, approximately 1.3 and 1.2 $W \cdot m^{-2} K^{-1}$, respectively, at vacuum pressures of 0.1 Pa. The GVIP and VIPPV samples exhibited center-of-pane U-values of 1.9 and 1.8 $W \cdot m^{-2} K^{-1}$, respectively, at the same vacuum pressure.

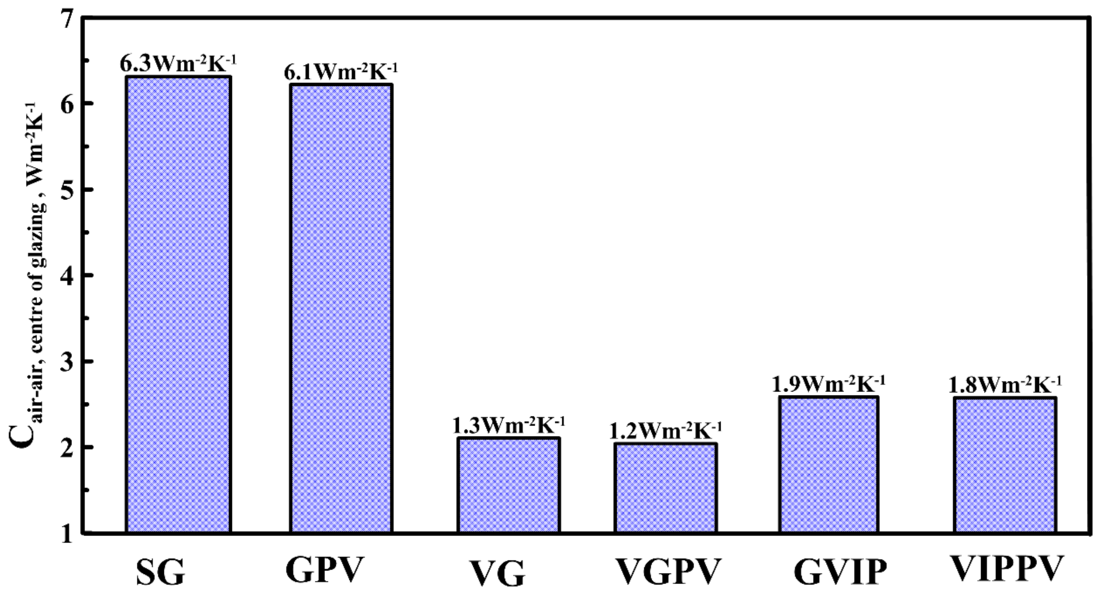

Fig. 15. Estimated (a) heat flux transfer and (b) total glazing U-value for the proposed systems under ASTM boundary conditions. The VG and VIP systems were simulated with a vacuum pressure of 0.1 Pa.

6. Conclusions

Advancements in, and integration of, progressive vacuum insulation technologies are believed to be one of the realistic solutions for converting domestic and commercial buildings into net ZEBs. Herein, the thermal and electrical performances of six progressive configurations for glazing systems have been compared. These include semi-transparent photovoltaic (GPV), VG, translucent vacuum insulation panel (GVIP), semi-transparent PV with VG (VGPV), semi-transparent PV with translucent vacuum insulation panel (VIPPV), and SG systems. These glazing systems were designed, constructed, and tested using a hot box calorimeter, and with and without application of simulated indoor solar radiation. The center-of-pane U-values, transient temperature variations of the inner and outer surfaces, open-circuit voltages, short circuit currents, fill factors, and the steady-state temperature contours (from the infrared camera) have been determined experimentally and compared. The moisture condensation patterns are also depicted for these systems. A 3D finite-volume heat transfer model is developed and validated with the experimental results, then used to compare the thermal performances of these systems under ASTM boundary conditions. The main conclusions are summarized in the following:

(1) The steady-state center-of-pane temperature differences are measured as 55 ºC, 32.5 ºC and 5 ºC for the VGPV, VIPPV, and GPV systems, respectively, with solar irradiation at the level of 1000 $W \cdot m^{-2}$.
(2) With a simulated solar radiation level of 1000 $W \cdot m^{-2}$, the steady-state open-circuit voltages are measured as 8.75, 8.25, and 7.85 V for GPV, VIPPV, and VGPV samples, respectively. These results show that the VGPV system achieved higher induced power and lower U-value relative to the VIPPV system.
(3) The FF of the semi-transparent PV samples decreases with increases in the simulated solar radiation, while the measured short circuit current ratio for these samples changes slightly under the same conditions.
(4) The predicted center-of-pane U-value for the VG, VGPV, VIPPV, and GPV samples with dimensions of 15 cm ×15 cm are predicted to be, and are validated as, 1.3, 1.2, 1.8, and 6.1 $W \cdot m^{-2} K^{-1}$, respectively, under ASTM boundary conditions.
(5) The results also show that the use of either the VGPV or VG system eliminates moisture condensation. It is concluded that VGPV and VIPPV systems generate comparatively less power but provide higher thermal insulation. It is recommended that future work should be done to develop and install independent self-powered intelligent EEW for buildings experiencing various climates.

Acknowledgement:

This research work was supported by Daiwa Anglo-Japanese Foundation (grant number12549/13360) (Project Leader: Dr Saim Memon and Project Partner: Dr Takao Katsura). The projects funders were not directly involved in the writing of this article. In support of open access research, all underlying article materials (data, models) can be accessed upon requesting via email to the corresponding author.

Nomenclature

q''	heat flux transfer [Wm^{-2}]
a	pillar diameter [m]
C	thermal conductance [$Wm^{-2} K^{-1}$]
FF	Fill factor [--]
h	convection heat transfer coefficient [$Wm^{-2}K^{-1}$]
k	thermal conductivity [$Wm^{-1}K^{-1}$]
l_v	VIP thickness [m]
P	pressure [Nm^{-2}]
P_{max}	maximum power [W]
s	pillars spacing [m]
S	source term in the energy equation [Wm^{-3}]
T	temperature [^{o} C]
U	thermal transmittance [$Wm^{-2}K^{-1}$]

Greek symbols

Δ	difference
δ	thickness [m]
ε	emissivity
σ	Stephan Boltzmann constant 5.67×10-8[$Wm^{-2}K^{-4}$]
∞,o	outdoor air
∞,in	indoor air

Subscripts

c	cold side of the HFM apparatus
g	glass
g,in	inner surfaces of the glazing's
g,o	outer surfaces of the glazing's
h	hot side of the HFM apparatus
oc	open circuit
sc	short circuit
v	vacuum space

References

[1] Peng J, Curcija DC, Thanachareonkit A, Lee ES, Goudey H, Selkowitz SE. Study on the overall energy performance of a novel c-Si based semitransparent solar photovoltaic window. Appl Energy 2019;242:854–72. doi:10.1016/j.apenergy.2019.03.107.

[2] Sun Y, Wilson R, Wu Y. A Review of Transparent Insulation Material (TIM) for building energy saving and daylight comfort. Appl Energy 2018;226:713–29. doi:https://doi.org/10.1016/j.apenergy.2018.05.094.

[3] Pan L, Yan R, Huang H, He H, Li P. Experimental study on the flow boiling pressure drop characteristics in parallel multiple microchannels. Int J Heat Mass Transf 2018;116:642–54. doi:10.1016/j.ijheatmasstransfer.2017.09.033.

[4] Ghosh A, Sarmah N, Sundaram S, Mallick TK. Numerical studies of thermal comfort for semi-transparent building integrated photovoltaic (BIPV)-vacuum glazing system. Sol Energy 2019;190:608–16. doi:10.1016/j.solener.2019.08.049.

[5] Brambilla A, Salvalai G, Imperadori M, Sesana MM. Nearly zero energy building renovation: From energy efficiency to environmental efficiency, a pilot case study. Energy Build 2018;166:271–83. doi:https://doi.org/10.1016/j.enbuild.2018.02.002.

[6] Huang H, Zhou Y, Huang R, Wu H, Sun Y, Huang G, et al. Optimum insulation thicknesses and energy conservation of building thermal insulation materials in Chinese zone of humid subtropical climate. Sustain Cities Soc 2020;52:101840. doi:https://doi.org/10.1016/j.scs.2019.101840.

[7] Ghosh A, Sundaram S, Mallick TK. Colour properties and glazing factors evaluation of multicrystalline based semi-transparent Photovoltaic-vacuum glazing for BIPV application. Renew Energy 2019;131:730–6. doi:https://doi.org/10.1016/j.renene.2018.07.088.

[8] Fung TYY, Yang H. Study on thermal performance of semi-transparent building-integrated photovoltaic glazings. Energy Build 2008;40:341–50. doi:https://doi.org/10.1016/j.enbuild.2007.03.002.

[9] Sun Y, Shanks K, Baig H, Zhang W, Hao X, Li Y, et al. Integrated semi-transparent cadmium telluride photovoltaic glazing into windows: Energy and daylight performance for different architecture designs. Appl Energy 2018;231:972–84. doi:10.1016/j.apenergy.2018.09.133.

[10] Qiu C, Yang H, Sun H. Investigation on the thermal performance of a novel vacuum PV glazing in different climates. Energy Procedia 2019;158:706–11. doi:10.1016/j.egypro.2019.01.190.

[11] Kang MG, Park N-G, Park YJ, Ryu KS, Chang SH. Manufacturing method for transparent electric windows using dye-sensitized TiO2 solar cells. Sol Energy Mater Sol Cells 2003;75:475–9. doi:https://doi.org/10.1016/S0927-0248(02)00202-7.

[12] Cuce E, Cuce PM. Optimised performance of a thermally resistive PV glazing technology: An experimental validation. Energy Reports 2019;5:1185–95. doi:10.1016/j.egyr.2019.08.046.

[13] Ghosh A, Sundaram S, Mallick TK. Investigation of thermal and electrical performances of a combined semi-transparent PV-vacuum glazing. Appl Energy 2018;228:1591–600. doi:https://doi.org/10.1016/j.apenergy.2018.07.040.

[14] Liu D, Sun Y, Wilson R, Wu Y. Comprehensive evaluation of window-integrated semi-transparent PV for building daylight performance. Renew Energy 2020;145:1399–411. doi:10.1016/j.renene.2019.04.167.

[15] Radwan A, Ookawara S, Ahmed M. Thermal management of concentrator photovoltaic systems using two-phase flow boiling in double-layer microchannel heat sinks. Appl Energy 2019;241:404–19. doi:https://doi.org/10.1016/j.apenergy.2019.03.017.

[16] Memon S, Farukh F, Eames PC, Silberschmidt V V. A new low-temperature hermetic composite edge seal for the fabrication of triple vacuum glazing. Vacuum 2015;120:73–82.

doi:https://doi.org/10.1016/j.vacuum.2015.06.024.

[17] Yang Z, Katsura T, Aihara M, Nakamura M, Nagano K. Development of numerical heat transfer and the structural model to design slim and translucent vacuum layer type insulation panels to retrofitting insulation in existing buildings. Energies 2017;10. doi:10.3390/en10122108.

[18] Memon S, Fang Y, Eames PC. The influence of low-temperature surface induction on evacuation, pump-out hole sealing and thermal performance of composite edge-sealed vacuum insulated glazing. Renew Energy 2019;135:450–64. doi:https://doi.org/10.1016/j.renene.2018.12.025.

[19] Fang Y, Hyde TJ, Arya F, Hewitt N, Eames PC, Norton B, et al. Indium alloy-sealed vacuum glazing development and context. Renew Sustain Energy Rev 2014;37:480–501. doi:https://doi.org/10.1016/j.rser.2014.05.029.

[20] Fang Y, Hyde T, Hewitt N, Eames PC, Norton B. Comparison of vacuum glazing thermal performance predicted using two- and three-dimensional models and their experimental validation. Sol Energy Mater Sol Cells 2009;93:1492–8. doi:https://doi.org/10.1016/j.solmat.2009.03.025.

[21] Eames PC. Vacuum glazing: Current performance and future prospects. Vacuum 2008;82:717–22. doi:https://doi.org/10.1016/j.vacuum.2007.10.017.

[22] Kalnæs SE, Jelle BP. Vacuum insulation panel products: A state-of-the-art review and future research pathways. Appl Energy 2014;116:355–75. doi:https://doi.org/10.1016/j.apenergy.2013.11.032.

[23] Alam M, Singh H, Brunner S, Naziris C. Experimental characterisation and evaluation of the thermo-physical properties of expanded perlite—Fumed silica composite for effective vacuum insulation panel (VIP) core. Energy Build 2014;69:442–50. doi:https://doi.org/10.1016/j.enbuild.2013.11.027.

[24] Schwab H, Stark C, Wachtel J, Ebert H-P, Fricke J. Thermal Bridges in Vacuum-insulated Building Façades. J Therm Envel Build Sci 2005;28:345–55. doi:10.1177/1097196305051794.

[25] Kwon JS, Jung H, Yeo IS, Song TH. Outgassing characteristics of a polycarbonate core material for vacuum insulation panels. Vacuum 2011;85:839–46. doi:10.1016/j.vacuum.2010.12.009.

[26] Kim J, Lee JH, Song TH. Vacuum insulation properties of phenolic foam. Int J Heat Mass Transf 2012;55:5343–9. doi:10.1016/j.ijheatmasstransfer.2012.05.051.

[27] Di X, Gao Y, Bao C, Hu Y, Xie Z. Optimization of glass fiber based core materials for vacuum insulation panels with laminated aluminum foils as envelopes. Vacuum 2013;97:55–9. doi:https://doi.org/10.1016/j.vacuum.2013.04.005.

[28] Mukhopadhyaya P, Kumaran MK, Normandin N, Reenen D van. Fibre-powder composite as core material for vacuum insulation panel. 9th Int Vac Insul Symp 17th 18th Sept 2009 R Inst Gt Britain London 2009.

[29] Choi B, Yeo I, Lee J, Kang WK, Song TH. Pillar-supported vacuum insulation panel with multi-layered filler material. Int J Heat Mass Transf 2016;102:902–10. doi:10.1016/j.ijheatmasstransfer.2016.06.032.

[30] Park KE, Kang GH, Kim HI, Yu GJ, Kim JT. Analysis of thermal and electrical performance of semi-transparent photovoltaic (PV) module. Energy 2010;35:2681–7. doi:https://doi.org/10.1016/j.energy.2009.07.019.

[31] Virtuani A, Pavanello D, Commission E, Friesen G. Overview of Temperature Coefficients of Different Thin Film Photovoltaic Technologies 2010. doi:10.4229/25thEUPVSEC2010-4AV.3.83.

[32] Huang J, Chen X, Yang H, Zhang W. Numerical investigation of a novel vacuum photovoltaic curtain wall and integrated optimization of photovoltaic envelope systems. Appl Energy 2018;229:1048–60. doi:10.1016/j.apenergy.2018.08.095.

[33] Skandalos N, Karamanis D. PV glazing technologies. Renew Sustain Energy Rev 2015;49:306–22. doi:https://doi.org/10.1016/j.rser.2015.04.145.

[34] Yang Z, Katsura T, Aihara M, Nakamura M, Nagano K. Investigation into window insulation retrofitting of existing buildings using thin and translucent frame-structure vacuum insulation panels. Energies 2018;11. doi:10.3390/en11020298.

[35] Katsura T, Radwan A, Yang Z, Nakamura M, Nagano K. Energy conservation using new structured-core and transparent vacuum insulation panels: Numerical simulation with experimental validation. Sol Energy 2019;193:885–905. doi:https://doi.org/10.1016/j.solener.2019.09.083.

[36] ANSYS FLUENT Theory Guide 2011.

[37] Arya F, Moss R, Hyde T, Shire S, Henshall P, Eames P. Vacuum enclosures for solar thermal panels Part 1: Fabrication and hot-box testing. Sol Energy 2018;174:1212–23. doi:https://doi.org/10.1016/j.solener.2018.10.064.

[38] Kwon JS, Jang CH, Jung H, Song TH. Effective thermal conductivity of various filling materials for vacuum insulation panels. Int J Heat Mass Transf 2009;52:5525–32. doi:10.1016/j.ijheatmasstransfer.2009.06.029.

[39] Fang Y, Eames PC, Norton B, Hyde TJ, Zhao J, Wang J, et al. Low emittance coatings and the thermal performance of vacuum glazing. Sol Energy 2007;81:8–12. doi:10.1016/j.solener.2006.06.011.

[40] Fang Y, Hyde TJ, Hewitt N. Predicted thermal performance of triple vacuum glazing. Sol Energy 2010;84:2132–9. doi:https://doi.org/10.1016/j.solener.2010.09.002.

[41] Kim J, Song TH. Vacuum insulation properties of glass wool and opacified fumed silica under variable pressing load and vacuum level. Int J Heat Mass Transf 2013;64:783–91. doi:10.1016/j.ijheatmasstransfer.2013.05.012.

[42] Strauss AJ, The AJS, Appliquee DP. The physical properties of cadmium telluride To cite this version : 1977;12:167–84.

[43] Radwan A, Ahmed M. The influence of microchannel heat sink configurations on the performance of low concentrator photovoltaic systems. Appl Energy 2017;206:594–611. doi:10.1016/j.apenergy.2017.08.202.

[44] Memon S, Eames PC. Predicting the solar energy and space-heating energy performance for solid-wall detached house retrofitted with the composite edge-sealed triple vacuum glazing. Energy Procedia 2017;122:565–70. doi:https://doi.org/10.1016/j.egypro.2017.07.419.

[45] Katsura T, Memon S, Radwan A, Nakamura M, Nagano K. Thermal performance analysis of a new structured-core translucent vacuum insulation panel in comparison to vacuum glazing: Experimental and theoretically validated analyses. Sol Energy 2020;199:326–46.

doi:https://doi.org/10.1016/j.solener.2020.02.030.

[46] Qin L, Lu X. Matlab/Simulink-Based Research on Maximum Power Point Tracking of Photovoltaic Generation. Phys Procedia 2012;24:10–8. doi:10.1016/j.phpro.2012.02.003.

[47] Duffie J a., Beckman W a. Solar Engineering of Thermal Processes (Google eBook). 2013.

[48] Anuforom AC, Gholap A V, Okeke CE. Variation of efficiency and short-circuit current of an array of silicon solar cells with intensity of solar radiation under tropical atmospheric conditions. Energy Convers Manag 1987;27:61–4. doi:https://doi.org/10.1016/0196-8904(87)90054-9.

[49] Lee KS, Chung YD, Park NM, Cho DH, Kim KH, Kim J, et al. Analysis of the current-voltage curves of a Cu(In,Ga)Se 2 thin-film solar cell measured at different irradiation conditions. J Opt Soc Korea 2010;14:321–5. doi:10.3807/JOSK.2010.14.4.321.

[50] Fang Y, Eames PC, Norton B, Hyde TJ. Experimental validation of a numerical model for heat transfer in vacuum glazing. Sol Energy 2006;80:564–77. doi:https://doi.org/10.1016/j.solener.2005.04.002.

[51] Collins RE, Simko TM. Current status of the science and technology of vacuum glazing. Sol Energy 1998;62:189–213. doi:10.1016/S0038-092X(98)00007-3.